

# Optimal excitation of AMOC decadal variability: Links to the subpolar ocean



Florian Sévellec<sup>a,\*</sup>, Alexey V. Fedorov<sup>b</sup>

<sup>a</sup> Ocean and Earth Science, National Oceanography Centre Southampton, University of Southampton, Southampton, UK

<sup>b</sup> Department of Geology and Geophysics, Yale University, New Haven, CT, USA

## ARTICLE INFO

### Article history:

Available online 4 March 2014

## ABSTRACT

This study describes the excitation of variability of the Atlantic Meridional Overturning Circulation (AMOC) by optimal perturbations in surface temperature and salinity. Our approach is based on a generalized stability analysis within a realistic ocean general circulation model, which extends the conventional linear stability analysis to transient growth. Unlike methods based on singular value decomposition, our analysis invokes an optimization procedure using Lagrangian multipliers, which is a more general approach allowing us to impose relevant constraints on the perturbations and use linear measures of the AMOC (meridional volume and heat transports).

We find that the structure of the optimal perturbations is characterized by anomalies in surface temperature or salinity centered in the subpolar regions of the North Atlantic off the east coasts of Greenland and Canada, south of the Denmark Strait. The maximum impact of such perturbations on the AMOC is reached after 7–9 yr. This is a robust result independent of the perturbations type, the optimization measures, the model surface boundary conditions, or other constraints. The transient growth involves the following mechanism: after the initial (positive) surface density perturbation reaches the deep ocean, it generates a cyclonic geostrophic flow that extracts a zonally-varying temperature anomaly from the mean temperature field in the upper ocean. In turn, the anomalous zonal temperature gradient induces, by thermal wind balance, a northward flow in the upper ocean and a southward flow in the deep ocean, thus strengthening the AMOC. Subsequently, the transient growth gives way to a decaying oscillation corresponding to a damped oceanic eigenmode with a period of about 24 yr. This mode is controlled by westward-propagating large-scale “thermal” Rossby waves, modifying the density field in the North Atlantic and hence the AMOC. Simple estimates show that realistic changes in salinity or temperature in the upper ocean (such as those due to the Great Salinity Anomaly) can induce AMOC variations of several Sverdrups via this mechanism, or 10–20% of the mean overturning. An idealized model is formulated to investigate the transient growth and highlight the role of mean convection in communicating surface density anomalies to the deep ocean.

© 2014 Published by Elsevier Ltd.

## 1. Introduction

Changes in the Atlantic Meridional Overturning Circulation (AMOC) represent an important aspect of climate variability and global change. Because this circulation transports a large amount of heat to northern high latitudes, its variability can affect global and European climate on timescales from decadal to centennial and longer (e.g. Gagosian, 2003). Consequently, the AMOC response to global warming, its variability and impacts have received enormous attention (for a recent review see Srokosz

et al., 2012). Potential mechanisms of this variability on decadal timescales, still poorly understood, are at the focus of the present study.

A vast observational program now monitors the strength of the AMOC on a daily basis (RAPID, Cunningham et al., 2007). However, the mechanisms of AMOC changes are still being debated. For instance, the causes of the recent dramatic decrease of the AMOC in the winter of 2009/2010 are not understood (Srokosz et al., 2012). Nor it is clear how the observed long-term trends in temperature and salinity in northern high latitudes are affecting or will affect the AMOC. For example, Hansen et al. (1999) and Mann et al. (1999) and subsequent studies discuss the increase of surface air temperatures in the Northern hemisphere over the past half-a-century. This change is paralleled by a reduction in ocean salinity in high latitudes in the North Atlantic since the mid-1970s

\* Corresponding author. Address: Ocean and Earth Science, University of Southampton, Waterfront Campus, European Way, Southampton SO14 3ZH, UK. Tel.: +44 2380 594850.

E-mail address: [florian.sevellec@noc.soton.ac.uk](mailto:florian.sevellec@noc.soton.ac.uk) (F. Sévellec).

(Dickson et al., 2002, 2003), possibly caused by an increase in precipitation in those regions (Josey and Marsh, 2005). Related changes in the deep ocean are noted by Curry et al. (2003) and Curry and Mauritzen (2005). Wang et al. (2010) argue that the long-term trends are such that the upper ocean in the subpolar North Atlantic is becoming cooler and fresher, whereas the subtropical North Atlantic becomes warmer and saltier, although decadal variability may differ from the long-term trends (Wang et al., 2010; Hátún et al., 2005; Thierry et al., 2008). Recently, Durack and Wijffels (2010) have demonstrated that the spatial structure of salinity changes in the Atlantic over the last 50 years agrees well with the expected changes in the hydrological cycle over the same time interval.

Such temperature and salinity changes in the upper ocean should modify ocean density field and therefore affect ocean circulation. In particular, the freshening of surface waters in the northern Atlantic has been broadly discussed as a key mechanism for the slowing-down of the AMOC (e.g. Broecker et al., 1990; Rahmstorf, 2002). In fact, “water hosing” experiments have been a useful tool for exploring the sensitivity of coupled or ocean general circulation models to external forcing in the northern Atlantic (e.g. Vellinga and Wood, 2002; Zhang and Delworth, 2005; Fedorov et al., 2004, 2007; Barreiro et al., 2008, for a review).

Another approach to assess the sensitivity of ocean circulation to surface perturbations involves adjoint methods (e.g. Marotzke et al., 1999). Using such an approach, Sirkes and Tziperman (2001) studied the sensitivity of ocean meridional heat transport at 24°N and found an oscillatory mode in the system with a centennial timescale. Bugnion et al. (2006a,b) studied the sensitivity of ocean circulation to surface forcing and identified critical sensitivity patterns in surface heat and freshwater fluxes and wind stress. More recently, Czeschel et al. (2010) have shown the existence of an interdecadal mode of variability in the North Atlantic by focusing on the AMOC meridional volume transport at 27°N. They speculated that trains of Rossby waves could explain the high sensitivity they found in the subpolar gyre region. Heimbach et al. (2011) also found a similar sensitivity of the AMOC to baroclinic Rossby waves at these latitude.

Although sensitivity studies with adjoint models are instructive, they do not necessarily provide insights into the adjustment mechanisms of the AMOC for example, or on why certain regions are critical for the AMOC sensitivity. Nor can they identify the initial conditions that would lead to the strongest change of the AMOC. These problems can be addressed by a related powerful method specifically designed to assess the sensitivity of ocean circulation to initial perturbations – the generalized stability analysis (GSA). This method is central to the present study. Unlike the classical linear stability analysis (e.g. Strogatz, 1994), the generalized stability analysis considers both the transient and asymptotic behavior of the system and, consequently, describes both transient and exponential growth (e.g. Farrell and Ioannou, 1996a; Nolan and Farrell, 1999).

GSA does not invoke any assumptions or approximation for ocean dynamics other than the linearization of the equations of motion with respect to the seasonally-varying basic state of the ocean. The assumption of linearity typically holds well for weak to moderate variability of ocean circulation (e.g. Tziperman, 1997).

GSA explicitly depends on the way one measures the system properties. Focusing on the AMOC strength for example, one can obtain the AMOC optimal perturbations, here defined as perturbations in temperature and salinity with such a spatial structure that modifies the overturning circulation most efficiently after an optimum time delay. Thus, this method allows studying the sensitivity of ocean circulation to the initial conditions and the details of ocean adjustment within an exogenous paradigm. While the generalized stability analysis also employs adjoint methods, it

yields initial conditions that can be used for time integrations and subsequent process studies, which goes farther than simple sensitivity studies using adjoint models.

Over recent decades, the generalized stability analysis has been applied to a number of problems ranging from mesoscale eddies (Rivière et al., 2001), El Niño-Southern Oscillation (ENSO, Moore et al., 2003; Sévellec and Fedorov, 2010), variations in tropical sea surface temperatures in the Atlantic (Zanna et al., 2010), western boundary currents (Farrell and Moore, 1992), to the ocean meridional overturning circulation.

Using a simple 3-box model, Tziperman and Ioannou (2002) showed the possibility of optimal growth for the thermohaline circulation (THC, a component of ocean circulation associated with large-scale buoyancy gradients). Sévellec et al. (2007) extended this work to a zonally-averaged latitude-depth model and developed an efficient method, based on a linear definition of the maximum THC change, to facilitate the computation of optimal perturbations in simple and complex ocean models, including planetary-geostrophic (Sévellec et al., 2009) and general circulation models (Sévellec et al., 2008). The latter study used a realistic global ocean model (OPA, Océan PARallélisé, Madec et al., 1998) with the seasonal cycle suppressed and focused on optimal surface salinity perturbations for the AMOC. More recently, Zanna et al. (2011) applied a method based on singular value decomposition to obtain AMOC optimal perturbations within an idealized version of the Massachusetts Institute of Technology general circulation model (MITgcm) using a rectangular, symmetric with respect to the equator basin with a flat bottom and no seasonal cycle. The findings of Sévellec et al. (2008), Sévellec et al. (2009), and Zanna et al. (2011) point to the roughly decadal timescale of the AMOC transient growth and the likely location of the optimal perturbations in the northern high latitudes of the Atlantic.

To test the importance of ocean–atmosphere interactions, Zanna and Tziperman (2005) studied the AMOC optimal perturbations in a simple coupled model (a two-layer latitude-depth ocean coupled to an energy balance model of the atmosphere). Tziperman et al. (2008) and Hawkins and Sutton (2009) studied optimal growth in coupled ocean–atmosphere general circulation models. To reduce the numbers of degrees of freedom in these coupled systems and make the problem computationally treatable, they had to truncate the essential dynamics to several leading Empirical Orthogonal Functions (EOFs). However, as shown by Farrell and Ioannou (2001), such a truncation cannot reproduce the model full sensitivity and underestimates the optimal growth. For this reason, here we will confine ourselves to a realistic ocean General Circulation Model (GCM), in which we will be able to use accurate linearized dynamics and evaluate the extent to which the AMOC transient growth can be reproduced solely by ocean processes.

Historically, for evaluating transient growth, GSA has used quadratic measures for the perturbations such as energy-based norms (e.g. Farrell and Ioannou, 1996a; Nolan and Farrell, 1999). However, as discussed by Sévellec et al. (2007), there are no objective reasons to restrict sensitivity studies solely to quadratic measures. In particular, in the present study, following Sévellec et al. (2007, 2008, 2009) and Sévellec and Fedorov (2010, 2013b), we will use linear measures, such as the AMOC volume or heat transport.

Optimal perturbations, when a quadratic measure is used, are given by the eigenvectors of the Singular Value Decomposition (SVD). In this study, since the optimality will be defined through linear measures, we will refer to the optimal perturbations as the Linear Optimal Perturbations (LOP). In general, the two methods (LOP and SVD) are not mutually exclusive; in fact they can be equivalent or partially equivalent. One difference is that for non-quadratic measures, the transient change induced by optimal perturbations can be related not only to the nonnormal dynamics of the system, but also to the oscillation phase changes.

An advantage of our broader approach is that the computed optimal initial perturbations can be used to determine the bounds on potential changes in the system. This is directly relevant to climate and ocean prediction. In fact, there is a subtle but important difference between the SVD and LOP approaches: SVD is often used to estimate error growth in the root-mean-square sense due to uncertainties in model initialization (Palmer, 1999), whereas LOPs can provide the actual bounds on the ensemble spread. We refer the reader to Sévellec et al. (2007) and subsequent papers for a discussion of our methodology and its similarities and differences with SVD.

In the present work, we apply the generalized stability analysis as proposed in Sévellec et al. (2008) but extend their study to a non-autonomous regime by taking into account the climatological seasonal cycle of the ocean (e.g. Farrell and Ioannou, 1996b). This improvement leads to a more accurate representation of ocean stratification and circulation in terms of strength and spatial structure. The linear measures of the maximum AMOC change are also as defined by Sévellec et al. (2008). When extending the previous work we will consider optimal surface perturbations in both salinity and temperature and examine the robustness of the optimal perturbations to differences in the problem formulation.

A key finding of our study is that the surface optimal initial perturbations for the AMOC have a spatial structure localized in the northern Atlantic and centered off the east coast of Greenland and Canada, just south of the Denmark Strait. The largest AMOC change is achieved within one decade or so (7–9 years) after the perturbations were applied. Furthermore, the optimal perturbations provide the most effective way to excite the least-damped interdecadal eigenmode of the AMOC described in a complementary study by Sévellec and Fedorov (2013a). These are robust results independent of the type of measures we use (e.g. the AMOC volume or heat transport), perturbation (temperature or salinity), the type of surface boundary conditions, or other constraints.

The particular location of the optimal perturbations is related, to a large degree, to the location of deep convection in the model. It is through the mean deep convection that surface density anomalies influence the deep ocean. Using an idealized model, we will show that the existence of the optimal delay critically depends on the fraction of the surface signal mixed into the deep ocean by deep convection. Density anomalies induced in the deep ocean are able to persist over a sufficiently long time, amplifying the transient change of the AMOC. The role of the deep ocean has been emphasized by Zanna et al. (2011) as well.

We should also note that while we talk about surface perturbations, we have to apply them over a layer of finite depth. In practice, this means applying the perturbations over the top level of the ocean GCM (10 m thickness).

The structure of the paper is as follows: in Section 2 we introduce the linearization procedure for the model's primitive equations of motion (crucial for deriving the tangent linear model and its adjoint). The climatological seasonal cycle of the full nonlinear model is also described. In Section 3 we discuss in detail the optimization method, the structure of the optimal perturbations and the physical mechanisms of the AMOC transient change. In Section 4, we use an idealized model to further elucidate the mechanisms involved in the transient change. In Section 5 we summarize the results and discuss directions for future work.

## 2. Configuration and seasonal cycle in the ocean GCM

### 2.1. Model configuration

The ocean GCM used in this study is OPA 8.2 (Madec et al., 1998) in its 2° global configuration (ORCA2, Madec and Imbard,

1996). There are 31 levels in the vertical – the model vertical resolution varies from 10 m at the surface to 500 m at depth. The rigid-lid approximation is used. The model is integrated on an Arakawa C-grid and the  $z$ -coordinates.

Although many models participating in the 5th Assessment Report (AR5) of the Intergovernmental Panel on Climate Change (IPCC) will use a 0.25° horizontal resolution in the ocean, our study takes advantage of a model with a lower resolution of 2° (note that the climate model of the Institut Pierre Simon Laplace, IPSL-CM5, has the OPA as its oceanic component with the same 2° resolution as part of AR5, see Marti et al., 2010). The main reason for using this relatively coarse resolution is to avoid small-scale baroclinic instability existing in eddy-permitting or eddy-resolving models. In a linear framework, such instability would not saturate and would dominate our calculations.

The present model configuration uses the following parameterizations: convection is parameterized by an increase in vertical diffusion when ocean stratification becomes unstable; double-diffusion is taken into account by two different terms for mixing temperature and salinity; eddy-induced velocities are described by the GM Gent and McWilliams (1990) approximation with a GM coefficient of  $2 \times 10^3 \text{ m}^2 \text{ s}^{-1}$ ; viscosity follows the turbulent closure scheme of Blanke and Delecluse (1993) and is a function of longitude, latitude and depth; and diffusion coefficients for temperature and salinity vary in longitude and latitude following Redi (1982) with isopycnal and diapycnal diffusivities set to  $2 \times 10^3 \text{ m}^2 \text{ s}^{-1}$  and  $1.2 \times 10^{-5} \text{ m}^2 \text{ s}^{-1}$ , respectively.

The linear and adjoint models are provided by the OPATAM code (the OPA Tangent Adjoint Model, Weaver et al., 2003). The tangent linear model is a linearization of the OPA's primitive equations of motions with respect to the ocean seasonally-varying basic state.

In the present study, we use either the flux boundary conditions (with surface heat and freshwater fluxes specified) or the mixed boundary conditions (with surface temperature restoring used in addition to freshwater fluxes). Mean fluxes at the ocean surface are computed by running the full nonlinear model forced with a combination of the prescribed climatological fluxes and restoring terms (restoring to the climatological seasonal cycle). This approach produces a realistic mean seasonal cycle for the linear and adjoint models, but reduces the damping and allows sea surface temperature anomalies to develop more easily (Huck and Vallis, 2001; Arzel et al., 2006; Sévellec et al., 2009), for details see below.

Several additional approximations have been introduced into the tangent-linear and adjoint models: viscosity coefficients in the momentum equations, tracer diffusivities in the temperature and salinity equations, and the GM advection velocity are calculated only for the basic ocean state – further variations in those coefficients are neglected.

### 2.2. Model seasonal cycle

The seasonally varying basic state of the ocean, also referred to as the annual model “trajectory”, is obtained by integrating the OPA model subject to the climatological surface boundary condition (i.e. varying with the annual cycle). For the forcing, we use surface heat fluxes estimated by the European Centre for Medium-Range Weather Forecasts (ECMWF) and averaged for the interval 1979–1993, wind stress measured by the European Remote Sensing satellite (ERS) and blended with the Tropical Atmosphere Ocean (TAO) data between 1993 and 1996, and an estimate of the climatological river runoff. In addition, we apply a surface temperature restoring to the Reynolds and Smith (1994) climatological values averaged from 1982 to 1989, together with a surface salinity restoring to the Levitus (1989) climatology. A mass restoring term to the Levitus climatological values of tem-

perature and salinity is applied in the Red and Mediterranean Seas. Starting with the Levitus climatology as the initial conditions, the model produces a quasi-stationary annual cycle of the ocean basic state after 200 years of integration.

We emphasize that in the experiments with the linear and ad-joint models the restoring term for surface temperature can be switched on or off, depending on the type of the boundary conditions used, while the restoring term for surface salinity always stays off.

The Atlantic meridional overturning circulation in the full ocean GCM (Fig. 1) is characterized by a northward mass transport above the thermocline, a southward return flow between 1500 and 3000 m, and a recirculation cell below 3000 m associated with Antarctic Bottom Water. The maximum volume transport of the AMOC is around 14 Sv, which is slightly below but still within

the errorbars of the observations (e.g.  $18 \pm 5$  Sv, Talley et al., 2003). The AMOC poleward heat transport reaches 0.8 PW at 25°N, whereas estimates from inverse calculations and hydrographic sections give roughly 1.3 PW at 24°N (Ganachaud and Wunsch, 2000).

As expected, the basic ocean state develops a strong meridional temperature gradient in the northern Atlantic, especially across the North Atlantic Current (NAC); it also has a salinity maximum at about 20°N (Fig. 1). The plot of barotropic streamfunction shows an intense subtropical gyre and a weaker subpolar gyre (the latter is centered at about 60°N). The two gyres are separated by the Gulf-stream and the NAC. Overall, the full nonlinear model produces a realistic seasonally-varying basic state of the ocean. Next, we will conduct a generalized stability analysis of this ocean state.

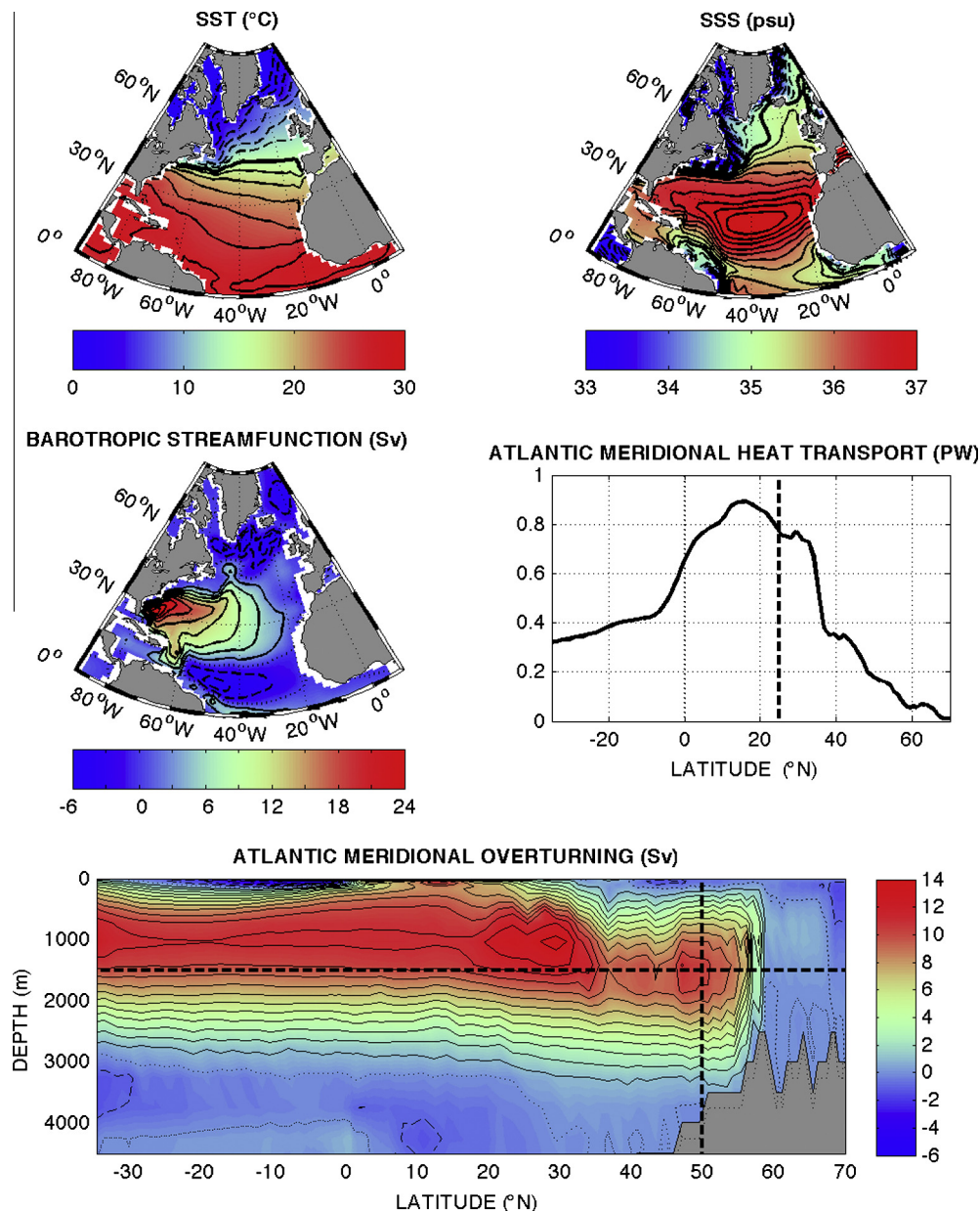


**Fig. 1.** The climatological basic state of the Atlantic ocean as reproduced by the full ocean GCM. (Top left) Sea surface temperature; contour intervals (CI) are 2 °C, the heavy line corresponds to 15 °C. (Top right) Sea surface salinity; CI are 0.25 psu, the heavy line corresponds to 35 psu. (Middle left) Barotropic streamfunction; CI are 3 Sv. (Middle right) The ocean meridional heat transport as a function of latitude. (Bottom) Zonally-averaged streamfunction showing the Atlantic meridional overturning circulation; CI are 1 Sv. Light plain, dashed and dotted lines in the two streamfunction plots indicate positive, negative and zero values; positive values correspond to clockwise rotation. In the bottom and middle-right panels, thick dashed lines indicate the particular locations where meridional volume and heat transports are estimated (MVT and MHT, to be used in the optimization problem).

### 3. Optimal initial perturbations

#### 3.1. Mathematical approach

The main goal of our calculations is to identify such initial perturbations in Sea Surface Temperature (SST) and Sea Surface Salinity (SSS) that can induce the largest change in the volume or heat transport of the ocean meridional overturning circulation after a time delay. In this sense they are referred to as the most efficient perturbations or the optimal perturbations. To achieve this goal, here we apply and extend the methodology originally proposed by Sévellec et al. (2007, 2008).

The prognostic equations of our model can be written as a general non-autonomous dynamical system:

$$d_t | \mathbf{U} \rangle = \mathcal{N}(| \mathbf{U} \rangle, t), \quad (1)$$

where  $\mathcal{N}$  is a time-dependent nonlinear operator and  $| \mathbf{U} \rangle$  is the ocean state vector consisting of all prognostic variables in the model. The state consists of three-dimensional fields of temperature, salinity, meridional and zonal velocity, and a two-dimensional field of barotropic streamfunction. Since we study a finite-dimensional vector space, we can also define a dual vector  $\langle \mathbf{U} |$  through the Euclidian scalar product  $\langle \mathbf{U} | \mathbf{U} \rangle$ .

We decompose the state vector as  $| \mathbf{U} \rangle = | \bar{\mathbf{U}} \rangle + | \mathbf{u} \rangle$ , where  $| \bar{\mathbf{U}} \rangle$  is the nonlinear annual trajectory and  $| \mathbf{u} \rangle$  is a perturbation. The time evolution of the perturbation follows a linear equation:

$$d_t | \mathbf{u} \rangle = \mathbf{A}(t) | \mathbf{u} \rangle, \quad \mathbf{A}(t) = \frac{\partial \mathcal{N}}{\partial | \mathbf{U} \rangle} \Big|_{| \bar{\mathbf{U}} \rangle}, \quad (2)$$

where  $\mathbf{A}(t)$  is the Jacobian matrix which is function of the annual trajectory  $| \bar{\mathbf{U}} \rangle$ . We also define an adjoint  $\mathbf{A}^\dagger(t)$  to the Jacobian matrix such that  $\langle \mathbf{a} | \mathbf{A} | \mathbf{b} \rangle = \langle \mathbf{b} | \mathbf{A}^\dagger | \mathbf{a} \rangle$ , where  $| \mathbf{a} \rangle$  and  $| \mathbf{b} \rangle$  are two anomalous state vectors, and  $\dagger$  refers to the adjoint defined through the Euclidian scalar product  $\langle \mathbf{a} | \mathbf{b} \rangle = \langle \mathbf{b} | \mathbf{a} \rangle$ .

One can integrate (2) to obtain an expression for the perturbation as a function of time (Farrell and Ioannou, 1996b):

$$| \mathbf{u}(t_2) \rangle = \mathbf{M}(t_2, t_1) | \mathbf{u}(t_1) \rangle, \quad (3)$$

where  $\mathbf{M}(t_2, t_1)$  is called the propagator of the linearized dynamics from time  $t_1$  to time  $t_2$ . Using similar numerical model and setting, Sévellec and Fedorov (2013a) showed that the propagator did not commute with its adjoint  $\mathbf{M}^\dagger(t_2, t_1) \mathbf{M}(t_2, t_1) \neq \mathbf{M}(t_2, t_1) \mathbf{M}^\dagger(t_2, t_1)$ . This result confirms the nonnormality of the linearized dynamics.

We will use and compare two different measures of the overturning for the subsequent optimization procedure – the ocean anomalous meridional volume and heat transports (MVT and MHT, respectively). They are evaluated at the locations in the Atlantic basin where their climatological values reach maximum values (1500 m deep at 50°N for MVT and at 25°N for MHT). These measures can be expressed as linear functions of the state vector anomaly,  $\langle \mathbf{F} | \mathbf{u} \rangle$ , and we will use one or the other as the cost function for the optimization.

To analyze perturbations in surface temperature and salinity (rather than velocity), we will also need to reduce our parameter space. To that end, we define a projector  $\mathbf{P}$  that connects the subspace of surface temperature or salinity to the full state vector as  $| \mathbf{u} \rangle = \mathbf{P} | \mathbf{u}' \rangle$ , where  $| \mathbf{u}' \rangle$  represents the surface temperature or salinity vector. In other words, the operator  $\mathbf{P}$  takes a full state vector and reduces it to a vector that has only surface temperature or salinity components. In practice, the operator extract temperature or salinity at the top level of the ocean GCM. This means that surface perturbations will be applied onto the 10 m thickness of the top model layer.

We define a norm for these vectors in terms of their density contribution as

$$\langle \mathbf{u} | \mathbf{S} | \mathbf{u} \rangle = \langle \mathbf{u}' | \mathbf{P}^\dagger \mathbf{S} \mathbf{P} | \mathbf{u}' \rangle = \langle \mathbf{u}' | \mathbf{N} | \mathbf{u}' \rangle = \frac{\iint ds \alpha^2 \text{SST}^2}{\iint ds} \text{ or } \frac{\iint ds \beta^2 \text{SSS}^2}{\iint ds}, \quad (4)$$

where SST and SSS are sea surface temperature and salinity components of the ocean state vector,  $\alpha$  and  $\beta$  are the thermal expansion and haline contraction coefficients,  $ds$  is a surface element,  $\mathbf{S}$  is a norm operator defined in the full state vector space, and  $\mathbf{N}$  is a norm operator defined in the subspaces of surface temperature or salinity. These norms describe the model departure from the mean annual trajectory in terms of density (averaged over the surface area of the basin). By definition, both of these norms are represented by invertible operators ( $\mathbf{S}$  and  $\mathbf{N}$ ).

In several computations we will require initial perturbations to have a spatial zero-mean for temperature (SST perturbations) or salinity (SSS perturbations). This condition distinguishes anomalies associated with an initial redistribution of heat or salt in the system and those induced by some external perturbation. To implement this constraint, we compute an average value of a tracer as

$$\langle \mathbf{C} | \mathbf{u} \rangle = \langle \mathbf{C} | \mathbf{P} | \mathbf{u}' \rangle = \frac{\iint ds \text{SST}}{\iint ds} \text{ or } \frac{\iint ds \text{SSS}}{\iint ds}, \quad (5)$$

where  $| \mathbf{C} \rangle$  is a vector whose scalar product with anomalous temperature or salinity fields gives spatial averages.

Finally, we define the Lagrangian function as:

$$\mathcal{L}(t_i, t_m) = \langle \mathbf{F} | \mathbf{u}(t_m) \rangle - \gamma_1 (\langle \mathbf{u}(t_i) | \mathbf{S} | \mathbf{u}(t_i) \rangle - 1) - \gamma_2 \langle \mathbf{C} | \mathbf{u}(t_i) \rangle, \quad (6)$$

where  $t_i$  is the initial time (the time when the optimal initial perturbation is applied),  $t_m$  is the maximization time (the time when the cost function reaches its maximum), and  $\gamma_1$  and  $\gamma_2$  are Lagrange multipliers.  $\gamma_1$  is the parameter associated with the normalization constraint

$$\langle \mathbf{u}(t_i) | \mathbf{S} | \mathbf{u}(t_i) \rangle - 1 = 0, \quad (7)$$

whereas  $\gamma_2$  is the parameter associated with the spatial zero-mean constraint on initial perturbations (i.e. initial perturbations should have a zero spatial mean):

$$\langle \mathbf{C} | \mathbf{u}(t_i) \rangle = 0, \quad (8)$$

Note that unlike the normalization constraint, the latter constraint is not actually required to obtain optimal perturbations. However, introducing this constraint will help us to test the robustness of the analysis later on.

From expression (6) and condition  $d\mathcal{L} = 0$  the optimal initial perturbations are computed as

$$| \mathbf{u}_{\{t_i, t_m\}}^{\text{opt}} \rangle = \pm \frac{1}{\gamma_1} \mathbf{P} \mathbf{N}^{-1} \mathbf{P}^\dagger [\mathbf{M}^\dagger(t_i, t_m) | \mathbf{F} \rangle - \gamma_2 | \mathbf{C} \rangle], \quad (9)$$

with

$$\gamma_1 = \sqrt{\langle \mathbf{F} | \mathbf{M}(t_m, t_i) \mathbf{P} \mathbf{N}^{-1} \mathbf{P}^\dagger \mathbf{M}^\dagger(t_i, t_m) | \mathbf{F} \rangle - 2\gamma_2 \langle \mathbf{C} | \mathbf{P} \mathbf{N}^{-1} \mathbf{P}^\dagger \mathbf{M}^\dagger(t_m, t_i) | \mathbf{F} \rangle + \gamma_2^2 \langle \mathbf{C} | \mathbf{P} \mathbf{N}^{-1} \mathbf{P}^\dagger | \mathbf{C} \rangle},$$

$$\gamma_2 = \frac{\langle \mathbf{C} | \mathbf{P} \mathbf{N}^{-1} \mathbf{P}^\dagger \mathbf{M}^\dagger(t_m, t_i) | \mathbf{F} \rangle}{\langle \mathbf{C} | \mathbf{P} \mathbf{N}^{-1} \mathbf{P}^\dagger | \mathbf{C} \rangle}.$$

These expressions give the full explicit solution of the optimization problem. It depends both on the initial time  $t_i$  and the maximization time  $t_m$ . In this study we will focus only on the effect of  $t_i$  and set  $t_m$  to the end of the year (31st of December). It turns out that the seasonal dependence of this solution is rather weak, which allows us to concentrate solely on decadal timescales. Consequently, we can define the time delay  $\tau = t_i - t_m$  as one of the key parameters of the problem (which gives the duration of transient change in the system). Note that the seasonal cycle in the model is still important since it ensures an accurate representation of the mean state of the ocean.

As mention in the introduction, another common method to obtain optimal perturbations is based on the singular value decomposition (Farrell and Ioannou, 1996a). Applying our approach (an optimization procedure with the use of Lagrange multipliers), but maximizing a norm instead of a linear measure of the AMOC would lead to an eigenvalue problem whose solutions are the singular vectors of the linearized dynamics and make the two methods equivalent.

Nevertheless, in the present and previous studies we choose to maximize a linear measure of the AMOC for two important reasons. Firstly, in a linear framework, a change in the AMOC intensity can be exactly expressed by a linear function of the state vector:  $\max(\psi) = \langle \mathbf{F} | \mathbf{U} \rangle = \langle \mathbf{F} | \bar{\mathbf{U}} \rangle + \langle \mathbf{F} | \mathbf{u}' \rangle$ , where  $\psi$  is the streamfunction representing the AMOC. Consequently, the cost function for the anomalous overturning is given by the anomalous overturning at the location of the mean overturning maximum:  $\langle \mathbf{F} | \mathbf{u}' \rangle = \psi' |_{\max(\bar{\psi})}$ , where  $\bar{\psi}$  and  $\psi'$  are the model climatological and anomalous streamfunctions. Secondly, using a linear measure yields an explicit solution of the problem, (9), which eliminates the necessity to solve an eigenvalue problem with much higher numerical costs. To see a more extensive discussion of this point we refer the reader to Sévellec et al. (2007).

### 3.2. Optimal transient change and the structure of perturbations

To test the robustness of our approach, we have conducted a suite of sixteen calculations (obtaining 16 different LOPs), each corresponding to different combinations of four major controlling factors for the problems, including:

1. The type of initial perturbations (SST or SSS).
2. The measure used in the maximization problem (MVT or MHT).
3. The type of boundary conditions (the flux boundary conditions or the mixed boundary conditions – FBC or MBC, respectively).
4. Whether the spatial zero-mean constraint on initial perturbations is imposed or not.

To obtain the most efficient initial perturbations, we first compute the transient changes in MVT or MHT induced by optimal initial perturbations for different time delays: from –1000 to 0 years. (Note that the validity of the linear assumption does not depend of the delay, but only on the amplitude of the perturbation.) A persistent feature of all these calculations is that the strongest transient change is achieved for time delays slightly shorter than one decade (Fig. 2). The AMOC response is much weaker for longer delays, so that in Fig. 2 we show only the range between –50 and 0 years. The spatial structure of the initial anomalies is shown in Fig. 3 and some of the key results are summarized in Tables 1 and 2.

In agreement with previous studies (Arzel et al., 2006; Sévellec et al., 2009), we find that one of the most important factors affecting the transient change is the choice of the boundary conditions.

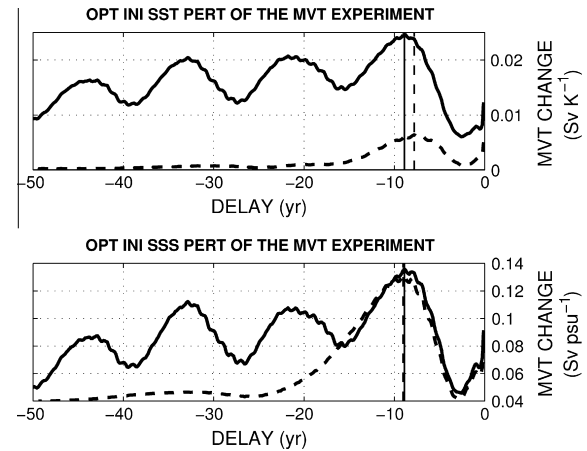


**Fig. 2.** The transient AMOC change induced by optimal initial perturbations as a function of time delay. Perturbations in surface temperature (top) and surface salinity (bottom) are considered. Meridional volume transport (MVT) is used as the measure of the overturning circulation, and the spatial zero-mean constraint applies. The computations are repeated for the flux and mixed boundary conditions – FBC (solid lines) and MBC (dashed lines). Thin vertical lines (solid or dashed) indicate the most efficient or “most optimal” delay in each case.

Whether we use the mixed boundary conditions (MBC, restoring SST to a specified atmospheric temperature and prescribing freshwater flux for salinity) or the flux boundary conditions (FBC, prescribing surface heat and freshwater fluxes for both temperature and salinity) dramatically affects the characteristics of the transient change, especially for SST perturbations, as described below. Note that for the SST restoring in MBC we use a coefficient of  $40 \text{ W m}^{-2} \text{ K}^{-1}$ .

Accordingly, changing the boundary conditions from FBC to MBC has several important consequences: first of all, the surface restoring term significantly reduces the impact of SST perturbations in general and the impact of both temperature and salinity perturbations for delays longer than 20 years (Fig. 2 and Table 1). While our computation with FBC exhibit a clear signature of decadal variability in ocean sensitivity, the oscillatory-like behavior is barely visible in the MBC calculations. In addition, the restoring term makes SST perturbations much less efficient than SSS perturbations – in the MBC calculations the amplitude of the transient change is roughly 150% greater for salinity anomalies than for temperature anomalies (when rescaled in terms of density).

In contrast, changing the measure used for optimization from MVT to MHT has relatively minor impacts. Calculations using MVT show the most efficient delay for inducing AMOC changes of 8.9 yr (Fig. 2). Calculations using MHT give a similar but slightly shorter delay of 7.8 yr (both results are for the flux boundary conditions). Thus, on decadal timescales the most efficient optimal delay depends on the optimization measure only weakly. The main difference is that in the MHT experiments, a relatively strong transient change in heat transport is also possible on timescales

**Table 1**  
Main characteristics of optimal transient change in different experiments. Note that experiments with or without spatial zero-mean constraint for temperature or salinity lead to nearly identical results. Consequently, this constraint is omitted from the table. The normalized growth is defined as  $\max_t(\langle \mathbf{u}(t) | \mathbf{S} | \mathbf{u}(t) \rangle) / (\langle \mathbf{u}(t=50 \text{ dy}) | \mathbf{S} | \mathbf{u}(t=50 \text{ dy}) \rangle)$ .

Optimization measure	Type of perturbations	FBC			MBC		
		Optimal time delay (yr)	Optimal change	Normalized growth	Optimal time delay (yr)	Optimal change	Normalized growth
MVT	SST	8.9	0.025 Sv K <sup>-1</sup>	1.5	7.8	0.006 Sv K <sup>-1</sup>	1.0
MVT	SSS	8.9	0.14 Sv psu <sup>-1</sup>	2.9	9.0	0.13 Sv psu <sup>-1</sup>	1.5
MHT	SST	7.8	0.0011 PW K <sup>-1</sup>	1.3	7.0	0.0003 PW K <sup>-1</sup>	1.0
MHT	SSS	7.8	0.0050 PW psu <sup>-1</sup>	3.1	8.1	0.0050 PW psu <sup>-1</sup>	1.7

**Table 2**  
Normalized projections of optimal initial perturbations (from different computations) onto each other, following (10).

Opt. measure	Opt. measure Pert. type	Spatial zero-mean constraint								No constraint							
		FBC				MBC				FBC				MBC			
		MVT SST	MVT SSS	MHT SST	MHT SSS	MVT SST	MVT SSS	MHT SST	MHT SSS	MVT SST	MVT SSS	MHT SST	MHT SSS	MVT SST	MVT SSS	MHT SST	MHT SSS
Spatial zero-mean constraint																	
MBC																	
MVT	SST	1.00															
MVT	SSS	0.99	1.00														
MHT	SST	0.95	0.93	1.00													
MHT	SSS	0.97	0.97	0.97	1.00												
FBC																	
MVT	SST	0.79	0.78	0.77	0.80	1.00											
MVT	SSS	0.97	0.97	0.91	0.94	0.79	1.00										
MHT	SST	0.80	0.79	0.80	0.82	0.98	0.80	1.00									
MHT	SSS	0.94	0.94	0.93	0.96	0.80	0.97	0.82	1.00								
No constraint																	
FBC																	
MVT	SST	0.99	0.99	0.94	0.96	0.79	0.96	0.80	0.94	1.00							
MVT	SSS	0.99	0.99	0.93	0.96	0.78	0.97	0.79	0.94	0.99	1.00						
MHT	SST	0.95	0.93	1.00	0.96	0.77	0.91	0.80	0.92	0.94	0.93	1.00					
MHT	SSS	0.97	0.97	0.96	1.00	0.80	0.94	0.82	0.96	0.97	0.97	0.96	1.00				
MBC																	
MVT	SST	0.79	0.78	0.77	0.80	1.00	0.79	0.98	0.79	0.79	0.78	0.77	0.80	1.00			
MVT	SSS	0.96	0.97	0.90	0.94	0.79	0.99	0.80	0.97	0.97	0.97	0.90	0.94	0.79	1.00		
MHT	SST	0.80	0.79	0.79	0.82	0.98	0.80	1.00	0.82	0.80	0.79	0.79	0.82	0.98	0.80	1.00	
MHT	SSS	0.94	0.94	0.92	0.96	0.79	0.97	0.82	1.00	0.94	0.94	0.92	0.96	0.80	0.97	0.82	1.00

lasting several months. However, the initial perturbations required for such an effect have small spatial scales and would lead to short-lived (seasonal) changes. Hereafter, we will focus solely on large-scale perturbations and longer-term (decadal) changes. Note that the very existence of an optimal timescale indicates that the transient change is not controlled solely by a single damped oscillatory mode, since in that case the curves in Fig. 2 would decay monotonically (Sévellec and Fedorov, 2013a).

In general, the shape of LOPs depends, albeit weakly, on the time delay. In the rest of the study, we will consider only the solutions of (9) corresponding to the “most optimal” or most efficient delay for each set of the controlling parameters (the vertical lines in Fig. 2). For brevity, we will refer to these solutions simply as the optimal perturbations.

For both MVT and MHT experiments with the flux boundary conditions, the AMOC transient changes induced by optimal SSS or SST perturbations, again rescaled in term of density, have similar magnitudes. However, salinity perturbations are slightly more efficient than temperature perturbations (Table 1). For example, in our MVT calculations an optimal density anomaly due to SSS generates a transient change 46% stronger than a similar density anomaly due to SST does. This difference is only 26% for the MHT calculations. These results imply that a freshening of surface waters is always a more efficient way to modify the ocean overturning circulation than a comparable warming.

The last controlling factor is whether we use or not the spatial zero-mean constraint for initial perturbations (the previous results were obtain with this condition). We find that using this constraint removes the spatial average from a variable, but does not affect the shape or the gradients within optimal initial perturbations. Nor does it change the optimal time delay. The relaxation of the zero-mean constraint actually increases the impact of optimal perturbations by a few percent.

Overall, for all 16 calculations the spatial structure of optimal initial perturbations remains nearly the same. The corresponding anomalies are located north of 45°N and extend along the east coast of Canada and Greenland into the Arctic. Their meridional

extent is greater than zonal. The optimal patterns are centered between the Reykjanes ridge and Greenland, south of the Denmark Strait (Fig. 3). There are just a few minor differences between the optimal patterns for the MVT (Fig. 3) and MHT experiments (not shown). For example, optimal initial perturbations for the MHT calculations develop a weak anomaly of an opposite sign to the main pattern (centered in the middle of the North Atlantic around 35°N, 35°W).

To compare different experiments, we compute the Normalized Projection (NP) between two initial perturbations as a measure of similarity between the perturbations

$$NP_{ij} = \frac{\iint ds SSD_i SSD_j}{\sqrt{\iint ds SSD_i SSD_i \iint ds SSD_j SSD_j}}, \quad (10)$$

where SSD is a surface density anomaly associated with an optimal perturbation and indices *i* or *j* indicates particular experiments amongst the sixteen we conducted. This diagnostic confirms that the shapes of the anomalies are extremely close (Table 2). It also shows that using the spatial zero-mean constraint barely changes the shape of the optimal initial perturbations. Thus, the optimal patterns are not affected by particular details of the experiments.

Note that the rather weak effect of the zero-mean constraint can be explained by the relatively small size of the optimal density anomaly as compared to the global surface area of the entire ocean. The compensating heat or salt fluxes needed to satisfy the zero-mean constraint are spread over such a big area that they do not significantly affect the optimal perturbations.

The robustness of the LOP patterns is a demonstration of the strong sensitivity of the AMOC to surface density anomalies in the subpolar regions of the North Atlantic. Such a close connection between density anomalies in those regions and the AMOC has been a cornerstone for the *ad hoc* approximation used in zonally averaged latitude-depth models (e.g. Marotzke et al., 1988; Wright and Stocker, 1991; Sévellec and Fedorov, 2011). Our results indirectly support the validity of such a simplified latitude-depth view of the AMOC dynamics.

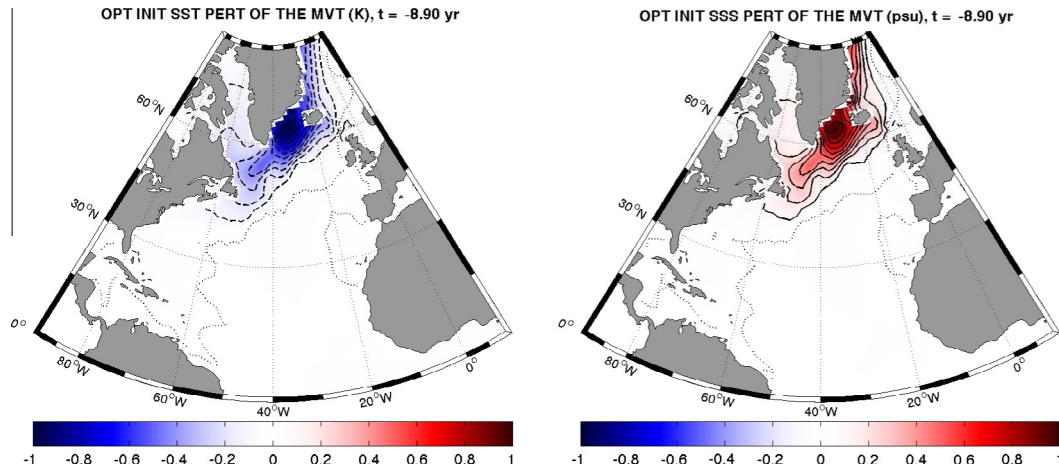


**Fig. 3.** The spatial structure of optimal initial perturbations in SST (left) and SSS (right) for the most efficient time delay. Subsequently, we will refer to these anomalies simply as the optimal initial perturbations. This figure is based on the MVT calculations with the flux boundary conditions and the spatial zero-mean constraint, yielding the most efficient delay of 8.9 years (indicated by solid vertical lines in Fig. 2). The structure of optimal perturbations in other experiments looks very similar (Table 2). The units are K for temperature and psu for salinity but could be multiplied by an arbitrary constant.

In the next section we will examine the physical mechanisms of the AMOC sensitivity to the optimal perturbations. We will demonstrate that this sensitivity is related to the evolution of surface density anomalies through successive processes involving (i) deep water formation and (ii) zonal baroclinic adjustment of the ocean.

### 3.3. Optimal transient change in different experiments

Given the strong similarities among the sixteen experiments, to understand the physical mechanism of the transient change we will concentrate on one experiment – the experiment with optimal perturbations in SST, using the flux boundary conditions, MVT as the measure of the overturning, and the spatial zero-mean constraint on initial anomalies (this was the very first calculation we conducted).

Let us consider a negative (cold) SST perturbation (within a linear framework, positive and negative perturbations lead to symmetrical results). After the initial surface anomaly is imposed (left of Fig. 3), it quickly undergoes convective adjustment. In the central region of the anomaly, the mean ocean mixed layer depth

reaches the bottom, which communicates surface perturbations to the deep ocean (Fig. 4).

Note that such a strongly nonlinear process as convection is difficult to treat fully within a linear framework since perturbations have to be small. Accordingly, the linearized model is simplified by using constant in time mixing coefficients estimated from the full nonlinear GCM, which in effect fixes the depth of the ocean mixed layer. Therefore, linear optimal perturbations cannot trigger or stop convection. Rather, temperature anomalies simply enhance or weaken convection (i.e. the amount of cold water mixed into the water column). From an oceanographer's perspective, the perturbations can lead to winters with more or less dense water formed (depending on the sign of the anomaly). However, they cannot result in winters without convection.

After the initial phase, the temperature anomaly is no longer located in the region of deep water formation, being advected southward by mean ocean circulation. At the same time, the ocean undergoes geostrophic adjustment that induces cyclonic circulation around the temperature anomaly. This circulation comprises anomalous northward flow on the right flank and anomalous southward flow on the left flank of the temperature anomaly. In

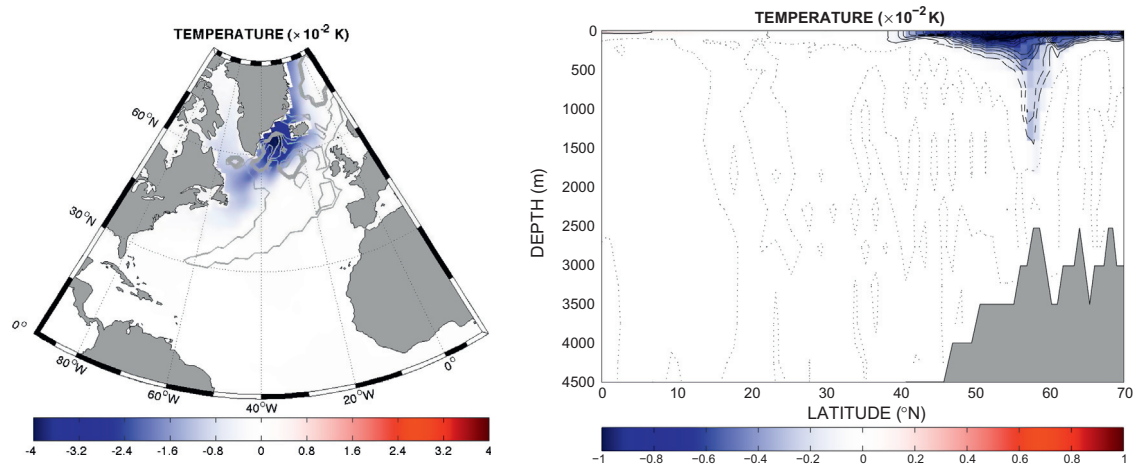


**Fig. 4.** (Left) As in the left panel of Fig. 3 but for temperature averaged over the top 240 m and with the mixed layer depth shown in grey contours (contour intervals are 500 m). (Right) A zonal average of the temperature anomaly that develops 100 days after the optimal SST perturbation was imposed. For the MVT calculations with the flux boundary conditions and the spatial zero-mean constraint. Note the spreading of the temperature anomaly into the deep ocean.



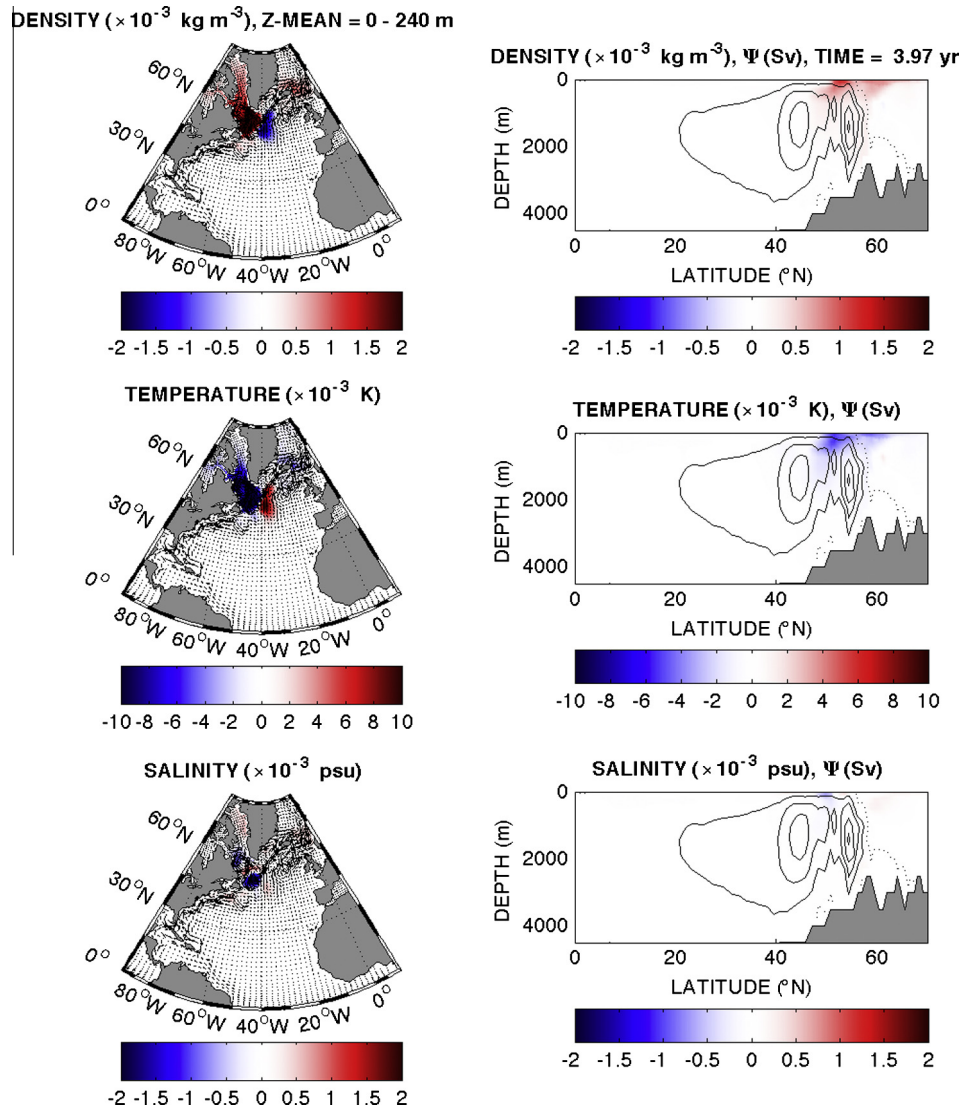


**Fig. 5.** Ocean response to the optimal initial SST perturbation four years after the perturbation was applied. From top to bottom: colors indicate anomalous density, temperature and salinity fields. (Left) Anomalies averaged over the top 240 m; arrows represent the horizontal flow. (Right) Zonally-averaged values; contour lines indicate the overturning streamfunction (contour intervals are  $5 \times 10^{-3}$  Sv). For the MVT calculations with the flux boundary conditions and the spatial zero-mean constraint. (For interpretation of the references to color in this figure legend, the reader is referred to the web version of this article.)

the upper ocean, this anomalous flow brings warm waters to the north along the right flank of the anomaly and cold waters to the south along the left flank. This process creates a warm SST anomaly to the right of the original temperature anomaly and a cold SST anomaly to the left (Fig. 5). These changes are equivalent to the westward propagation of the original anomaly as a “thermal” Rossby wave. The mean meridional temperature gradient is critical for this propagation (e.g. Sévellec and Fedorov, 2013a).

However, this process is not a simple propagation of temperature anomalies. The part of the original temperature perturbation that has reached the deep ocean also contributes to the anomalous flow (by thermal wind balance) and thus to temperature anomalies in the upper ocean. The deep-ocean temperature anomalies are able to extract energy from the mean meridional thermal gradient on even timescales longer than the temperature anomaly in the upper ocean can, since in the absence of strong thermal gradients or currents in the deep ocean anomalies propagate very slowly. At this stage, the temperature anomaly has grown,  $\max(\langle \mathbf{u}(t) | \mathbf{S} | \mathbf{u}(t) \rangle) > \langle \mathbf{u}(t = 50 \text{ dy}) | \mathbf{S} | \mathbf{u}(t = 50 \text{ dy}) \rangle$ , in most of the experiments (Table 1), except in the case of SST perturbations under MBC.

The efficient stimulation of upper-ocean anomalies by the deep ocean is consistent with the previous numerical and analytical analyses of the dominant modes of ocean adjustment relevant to the AMOC (Sévellec and Fedorov, 2013a). Different dynamics in the deep and upper oceans are in part responsible for the nonnormality of the transient change (Sévellec and Fedorov, 2013b). The importance of the deep ocean for the ocean response to surface initial perturbations will be discussed in more detail in Section 4.

By the time of the maximum change (Fig. 6), there develops a dipole-like temperature anomaly in the upper ocean with a strong zonal gradient (Fig. 7) that sustains a surface northward flow. This anomalous upper-ocean current is compensated at depths by a southward flow in accordance with thermal wind balance and the baroclinicity condition that should hold for sufficiently long timescales. The dipole-like temperature anomaly develops roughly 8–9 years after the initial anomaly was imposed leading to the strongest intensification of the AMOC. Ocean changes at this time also involve the intensification of western boundary currents in regions outside the northern Atlantic (such as the North Brazilian Current and the Gulfstream, Fig. 7).

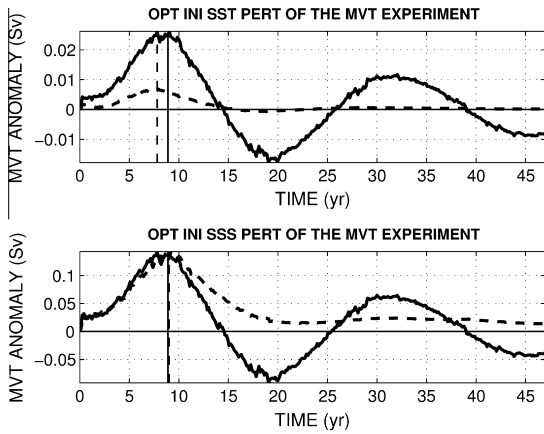


**Fig. 6.** The evolution of meridional volume transport (MVT) for two types of optimal surface perturbations (SST and SSS). Calculations have been repeated for the flux and mixed boundary conditions – FBC (solid lines) and MBC (dashed lines), respectively, cf. Fig. 2. The spatial zero-mean constraint applies.

In summary, we can interpret the transient change as a process in which anomalous flow in the upper ocean extracts temperature anomalies from the mean temperature field. In contrast, in the

deep ocean (below 1000 m or so) mean thermal gradients are weak, so that any new temperature anomalies should be confined to the upper ocean. By a similar argument, the newly generated upper-ocean density anomalies – the main dynamic factor of the change – should be controlled mainly by temperature (Fig. 7). The meridional salinity gradient is simply too weak in the ocean ( $|\alpha\partial_y\bar{T}| > |\beta\partial_y\bar{S}|$ ), and so are the newly generated salinity anomalies (which partially compensate the effect of temperature on density).

After the AMOC transient growth reaches its maximum, the subsequent evolution of temperature anomalies and the AMOC is controlled by the damped interdecadal eigenmode of the ocean dynamics in the Atlantic as described by Sévellec and Fedorov (2013a); also see Huck et al. (1999), de Verdière and Huck (1999), te Raa and Dijkstra (2002), and Sévellec et al. (2009) who studied a similar interdecadal eigenmode in more idealized systems. In the description of the interdecadal mode by Sévellec and Fedorov (2013a), temperature anomalies propagate westward as large-scale thermal planetary waves (“thermal” Rossby waves). The propagation speed is determined by the interplay between the westward geostrophic self-advection due to the mean meridional temperature (density) gradient, eastward advection due to the mean currents, and westward propagation due to the  $\beta$ -effect. The sign of the zonal temperature gradient induced by the

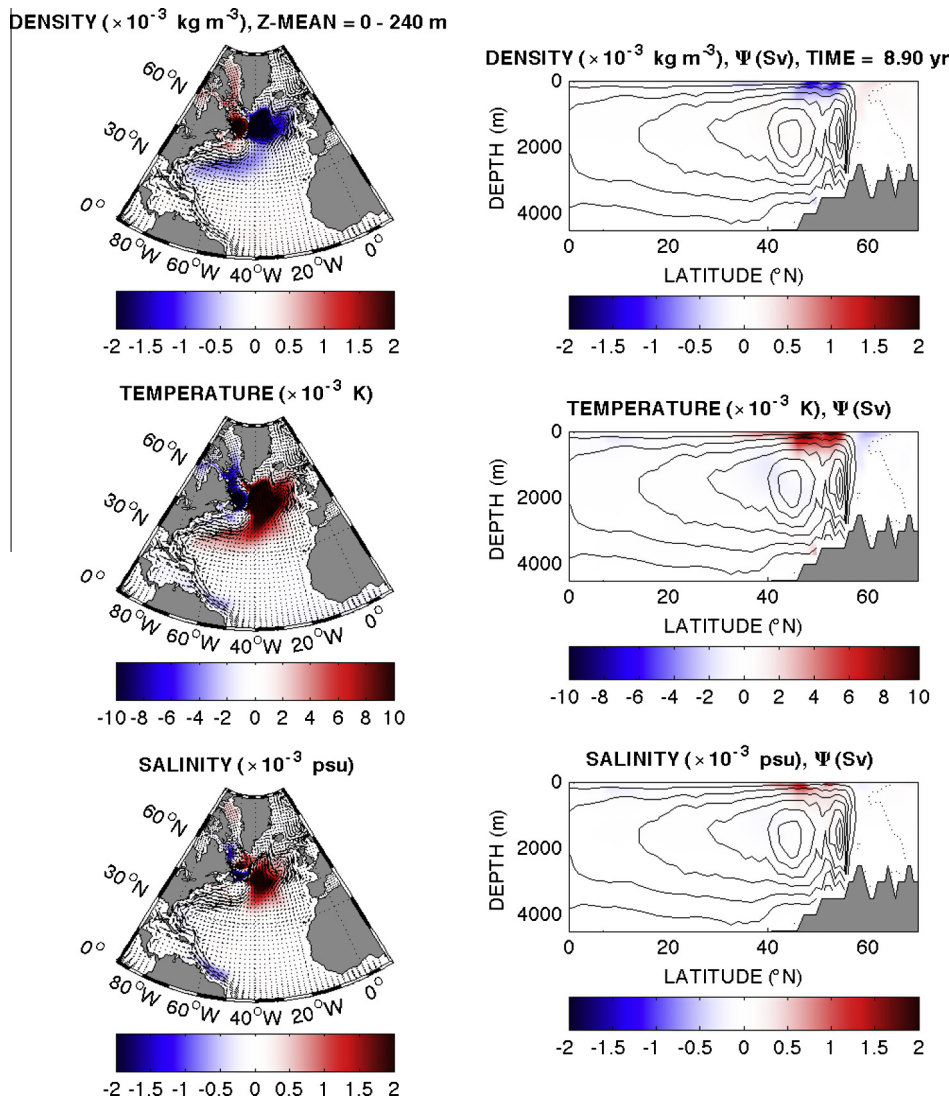


**Fig. 7.** As in Fig. 5 but 8.9 years after the optimal perturbation was applied. The anomalies in various fields are shown at the exact moment when meridional volume transport (MVT) reaches its maximum.

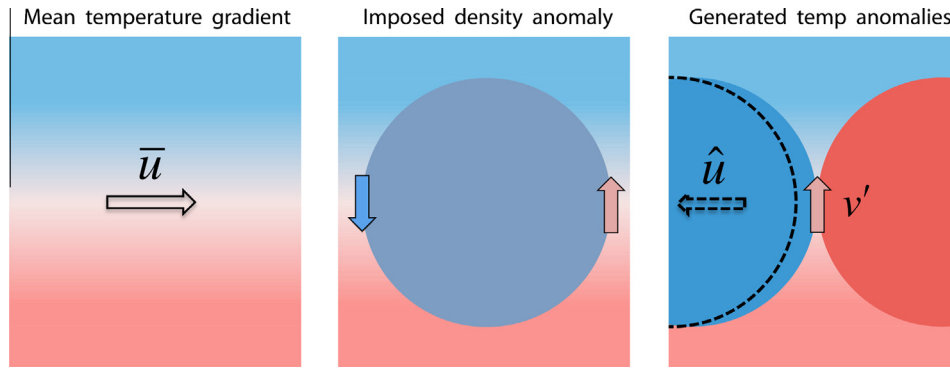


**Fig. 8.** A schematic of the transient change mechanism. Blue and red colors represent warmer and colder temperatures, respectively. Light colors show the mean temperature distribution in the upper ocean whereas heavier colors indicate temperature anomalies. Purple indicates a density anomaly. (Left) The mean meridional gradient of temperature and the corresponding eastward zonal velocity ( $\bar{u}$ ). (Middle) The imposed positive density anomaly and the generated geostrophic cyclonic flow. This flow extracts cold and warm temperature anomalies from the mean temperature field. (Right) The generated temperature anomalies and the northward surface flow ( $v'$ ) given by thermal wind balance. The effective westward propagation of the anomalies ( $\hat{u}$ ) is also shown. (For interpretation of the references to color in this figure legend, the reader is referred to the web version of this article.)

alternating temperature anomalies determines the sign of AMOC anomalies – intensification or weakening.

Analyzing other experiments confirms the previous description of the transient change mechanism but also gives us additional insights. Firstly, we find that a similar transient growth would occur if instead of a cold SST anomaly we imposed a positive SSS anomaly. Such a salinity anomaly would result in a positive density anomaly, leading to similar dynamical changes as described previously and generating a warm temperature anomaly on the right flank and a cold temperature along the left flank of the initial density anomaly (Fig. 8). Thereafter, dynamics are largely controlled by temperature changes rather than salinity. The fact that similar temperature anomalies can be generated either by optimal initial temperature or initial salinity perturbations is a consequence of the nonnormal character of the transient change.

Secondly, despite the rather different measures of the AMOC strength used in the computations (we evaluate MHT at 25°N and MVT at 50°N), the optimal perturbations and the transient behavior are almost identical for the two measures. This fact emphasizes the dominance of large-scale dynamics over particular details of the optimal excitation of the AMOC. This also suggests that the most efficient way to modify the meridional heat transport is by modifying meridional volume transport rather than the ocean thermal structure.

Finally, our computations using the mixed boundary conditions demonstrate that SST restoring influences the initial stages of the transient change only for the optimal SST perturbations, and not for salinity perturbations. However eventually, with the SST restoring, AMOC variations (Fig. 6) become strongly damped regardless of the type of the initial perturbation because it is the newly generated temperature anomalies that control the subsequent changes. Nevertheless, a weak signature of the damped interdecadal mode is still visible in the plots of the AMOC evolution under the mixed boundary conditions.

#### 4. Idealized model

##### 4.1. Model formulation and eigenmodes

In this section, we formulate an idealized model of ocean dynamics to highlight the fundamental mechanism of the transient change and its nonnormal characteristics. The setting of the model follows that of Sévellec and Fedorov (2013a). However, whereas the previous study investigated the existence and properties of the least-damped, interdecadal AMOC eigenmode, here we focus

on how this particular mode can be excited most efficiently. This latter problem deals with a transient behavior of the system and requires a different approach in view of the system nonnormality.

The idealized model describes the linear dynamics of the ocean GCM with several approximations applied. For simplicity, given a decadal timescale of the transient change, we neglect the seasonal cycle and consider the system as autonomous. Also, the large spatial scale of the problem allows us to reduce the momentum equations to geostrophic balance on a  $\beta$ -plane (the planetary-geostrophic regime, e.g. de Verdière, 1988).

The model treats anomalies in temperature  $T'$  and salinity  $S'$  (chosen to be functions of time  $t$  and the zonal coordinate  $x$ ) on two ocean levels – the top level (of depth  $h$ ) and the deep level (Fig. 9). The evolution of these anomalies follows a set of advection–diffusion equations as in the ocean GCM. To simplify the mathematical procedure of the analysis, meridional variations in  $T'$  and  $S'$  are neglected. The zonal extent of the model basin is  $W$ ; its full depth is  $H$ .

The equations are linearized with respect to the mean state of the ocean. In particular, at the upper level we impose the mean zonal flow  $\bar{u}$  and mean temperature and salinity gradients. These gradients have meridional and vertical components:  $\partial_y\{\bar{T}, \bar{S}\}$  and  $\partial_z\{\bar{T}, \bar{S}\}$ , where  $y$  and  $z$  are the meridional and vertical coordinates, and  $\bar{T}$  and  $\bar{S}$  are mean temperature and salinity, respectively. The mean zonal gradients of temperature and salinity are neglected. The mean gradients in the equations are approximated by simple constants obtained from the GCM output (Table 3). In the deep ocean those constants are set to zero.

For the prognostic variables of the model, we choose  $T'_u$  and  $S'_u$ , and  $T'_d$  and  $S'_d$  – temperature and salinity anomalies in the upper and deep oceans, respectively. These variables evolve according to linearized advective-diffusion equations with horizontal diffusivity  $\kappa$ :

$$\partial_t T'_u = -\bar{u}\partial_x T'_u - v'_u\partial_y \bar{T} - w'_u\partial_z \bar{T} + \partial_x(\kappa\partial_x T'_u), \quad (11a)$$

$$\partial_t S'_u = -\bar{u}\partial_x S'_u - v'_u\partial_y \bar{S} - w'_u\partial_z \bar{S} + \partial_x(\kappa\partial_x S'_u), \quad (11b)$$

$$\partial_t T'_d = \partial_x(\kappa\partial_x T'_d), \quad (11c)$$

$$\partial_t S'_d = \partial_x(\kappa\partial_x S'_d), \quad (11d)$$

where  $v'_u$  and  $w'_u$  are the meridional and vertical velocity in the upper ocean, respectively.

The system is closed using thermal wind balance with a baroclinicity condition for the meridional velocity, a linear equation of state for seawater, a continuity equation, and the rigid-lid approximation:

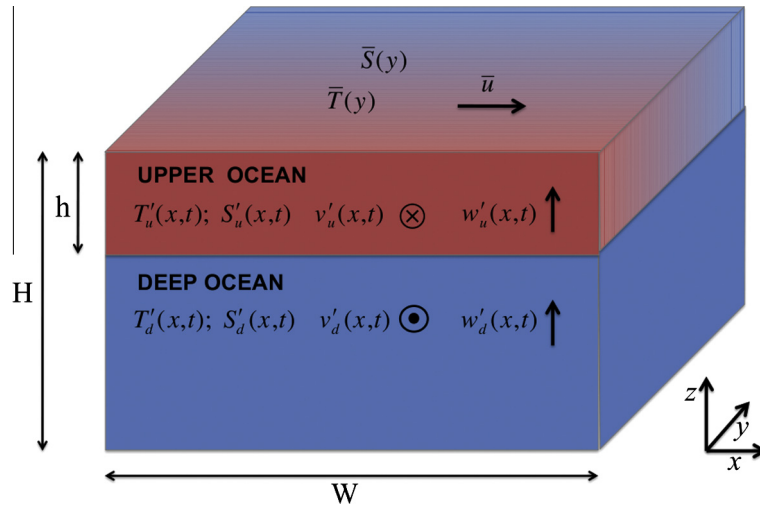


**Fig. 9.** A schematic of the idealized model (cf. Fig. 8). The two levels of the model represent the upper and deep ocean. The prognostic variables are temperature and salinity at each level ( $T'_u, S'_u, T'_d$ , and  $S'_d$ , respectively). The four diagnostic variables are meridional and vertical velocities, also at each level ( $v'_u, w'_u, v'_d$ , and  $w'_d$ ). The model free parameters are the upper-ocean thickness  $h$ , the total ocean depth  $H$ , the zonal extent of the Atlantic basin  $W$ , the mean meridional flow  $\bar{u}$ , and the mean temperature and salinity fields ( $\bar{T}$  and  $\bar{S}$ ). For  $\bar{T}$  and  $\bar{S}$  we choose linear functions of  $y$  at the top level and constants at the deeper level. Those constants are equal to the values of temperature and salinity in the upper ocean at the northern boundary of the basin. Implicitly, we assume a nonzero vertical stratification in the upper layer that can support baroclinic Rossby waves due to the  $\beta$ -effect. The dependence of the model variables on spatial coordinates (zonal –  $x$ , meridional –  $y$ , and vertical –  $z$ ) and time  $t$  is shown in brackets. Colorscale (blue to red) represents mean temperature variations (colder to warmer). (For interpretation of the references to color in this figure legend, the reader is referred to the web version of this article.)

**Table 3**  
Parameters of the idealized model.

$h$	1200 m	Model top level thickness
$H$	4500 m	Total ocean depth
$W$	60°	Basin zonal size
$L$	60°	Basin meridional size
$\kappa$	$2 \times 10^3 \text{ m}^2 \text{ s}^{-1}$	Horizontal tracer diffusivity
$g$	$9.8 \text{ m s}^{-2}$	Acceleration due to gravity
$f$	$10^{-4} \text{ s}^{-1}$	Coriolis parameter
$\beta_f$	$1.5 \times 10^{-11} \text{ m}^{-1} \text{ s}^{-1}$	Gradient of the Coriolis parameter (planetary vorticity gradient)
$\alpha$	$2 \times 10^{-4} \text{ K}^{-1}$	Thermal expansion coefficient
$\beta$	$7 \times 10^{-4} \text{ psu}^{-1}$	Haline contraction coefficient
$\Delta T$	–15 K	Mean meridional temperature contrast
$\Delta S$	–1.5 psu	Mean meridional salinity contrast
$\bar{u}$	$2.5 \times 10^{-2} \text{ m s}^{-1}$	Mean zonal velocity in the upper ocean
$p$	0.15	Mixing parameter (the fraction of the initial anomaly mixed into the deep ocean)

$$\partial_z v' = \frac{g}{f} (\alpha \partial_x T' - \beta \partial_x S'), \quad (12a)$$

$$\int_{-H}^0 v' dz = 0, \quad (12b)$$

$$\partial_y v' + \partial_z w' = 0, \text{ with } w'|_{z=0} = 0 \quad (12c)$$

where  $v'$  and  $w'$  are the meridional and vertical velocities; both are functions of  $x, y$  and  $z$ .  $f$  is the Coriolis parameter,  $g$  – the acceleration of gravity,  $\alpha$  – the thermal expansion coefficient,  $\beta$  – the haline contraction coefficient (the numerical values of these parameters are given in Table 3). To obtain the meridional and vertical velocity in the upper level ( $v'_u$  and  $w'_u$ , respectively), we vertically discretized on the upper and deep levels the latter set of equations using the Arakawa C-grid (together with simple linear interpolations between the missing values, if needed).

Applying the Fourier transform in  $x$  to  $T'_u, T'_d, S'_u$  and  $S'_d$  yields, after some algebra, equations for the corresponding Fourier coefficients  $T_{cn}^u, T_{sn}^d, T_{cn}^u, T_{sn}^d, S_{cn}^u, S_{sn}^d, S_{cn}^u, S_{sn}^d$ , where  $n$  indicates the wave number,  $u$  and  $d$  stand for the upper and deep levels, and  $c$  and  $s$  – for cosine and sine. These Eqs. (A1) are summarized in Appendix A and used in the analysis below. As shown by Sévellec

and Fedorov (2013a), this idealized model is able to reproduce the dynamical behavior of the linear tangent and adjoint versions of the ocean GCM with the flux boundary conditions. Those authors also discussed the horizontal boundary conditions required for such a model.

Because of the model simplicity, we are able to compute the Jacobian matrix and the eigenmodes of the model and its adjoint analytically, which facilitates the understanding of the transient growth. Accordingly, the idealized model has eight eigenvectors ( $|\mathbf{u}_{1-8}\rangle$ ) corresponding to eight eigenvalues ( $\lambda_{1-8}$ ) as shown in Appendix A.

There exist two oscillatory modes in the system (related to two pairs of complex eigenvalues). The first mode is described by  $|\mathbf{u}_{1,2}\rangle$  (Eqs. A2 and A5 of Appendix A, also see Sévellec and Fedorov, 2013a). It is an interdecadal, temperature-dominated mode with a period  $\Pi = 25.5$  yr for  $n = 1$ . Salinity in this mode tends to compensate the effect of temperature on density, but only partially. Temperature anomalies associated with this mode propagate westward (upstream of the mean flow). The westward propagation is due to the effective advection of anomalies on the mean meridional temperature gradient (geostrophic self-advection) and the  $\beta$ -effect. The period equals twice the time needed for the anomalies to cross the basin.

The other oscillatory mode is described by  $|\mathbf{u}_{3,4}\rangle$  (Eqs. A3 and A5). This mode, with a period of 12 yr, is a spiciness mode passively advected by the mean flow. It has no impact on the density field and hence ocean circulation.

Both oscillatory modes have signatures only in the upper ocean. Their e-folding decay timescale of 36 yr is set by horizontal diffusion. The four other eigenmodes ( $|\mathbf{u}_{5-8}\rangle$ ) are purely damped, with the same diffusive decay timescale of 36 yr (Eq. A4).

#### 4.2. Optimal perturbations and the transient change mechanism

Next, we conduct a general stability analysis of the idealized system (Eqs. 9) similar to our analysis of the ocean GCM (Sections 33.1 and 33.2). Since variations in meridional heat transport in the GCM computations are largely related to changes in volume

transport (i.e. linear MHT changes are related to anomalous advection of mean temperature rather than mean advection of temperature anomalies), we will focus solely on meridional volume transport. That is, we will search for the optimal initial perturbations leading to the maximum change of MVT.

The details of these calculations are summarized in Appendix A, but an important new element of the present approach (different from Sévellec and Fedorov, 2013a) is that here we introduce a parameterization of the ocean mean deep convection and its effect on the imposed anomalies. In particular, we take into account the injection of surface waters into the deep ocean evident in the GCM experiments (Fig. 4). This is done by adding an implicit constraint to the optimization problem that allows for an instantaneous redistribution of initial temperature or salinity anomalies between the model top and deep layers with a fixed ratio of  $p$ . This mixing parameter, as included in the projectors  $\mathbf{P}_{id}^{SST}$  or  $\mathbf{P}_{id}^{SSS}$  (Eqs. A8), indicates how much water is injected into the deep ocean from the surface right after initial perturbations are imposed. It is defined in such a way that  $p=0$  means no deep mixing at all, whereas  $p=1$  means that the initial heat or salinity anomaly becomes fully mixed between the two layers.

The results of the optimization analysis confirm that the mixing parameter  $p$  is indeed critical for the transient change. The idealized model shows transient growth after a delay of 9–10 yr (Fig. 10), consistent with the GCM results (Fig. 2); however, optimal delays exist only for  $p \geq 0.13$ , see Fig. 11. The magnitudes of the AMOC transient change and perturbation growth increase for higher values of  $p$  when more of the initial surface anomaly is mixed between the two layers. Thus, the existence of an optimal delay requires a sufficiently strong stimulation of the deep ocean, which emphasizes the importance of the deep ocean for the non-normal growth.

The role of the deep ocean can be understood by looking at the eigenmodes of the system and their biorthogonal (the latter measure the sensitivity of the former). According to the theories of nonnormal systems (e.g. Farrell and Ioannou, 1996a), the most efficient stimulation of an eigenmode can be done by its biorthogonal, i.e. by a mode orthogonal to all other eigenmodes. While a change of MVT can occur only when  $|\mathbf{u}_{1,2})$  and  $|\mathbf{u}_5)$  are stimulated (see Appendix A for their full expressions), the sensitivity of these

two eigenvectors are controlled by density anomalies in the deep ocean ( $|\mathbf{u}_{1,2})$  and  $|\mathbf{u}_5)$ , respectively). Consequently, deep-ocean density anomalies are more efficient in extracting temperature anomalies in the upper ocean than upper-ocean density anomalies (as discussed previously by Sévellec and Fedorov, 2013b). This is because density anomalies in the deep ocean (with vanishing stratification and mean flow) do not propagate and are able to persist much longer.

Now we are ready to discuss the mechanism of transient growth in the idealized model. We find that the structure of the optimal initial perturbations in the model is shifted slightly eastward with respect to the middle of the basin (Fig. 12, dashed line, top left or right panels). As a result, optimal perturbations leading to an increase in MVT, for example, correspond to predominantly negative SST anomalies or positive SSS anomalies.

When a negative SST anomaly is imposed, it generates a geostrophic southward flow in the western part of the basin and a northward flow in the eastern part. This anomalous flow acts on the mean meridional temperature and salinity gradients in the upper ocean to modify the initial density anomaly. The mean meridional temperature gradient is dominant in this process, and the anomalous geostrophic flow induces a negative temperature anomaly in the west and a positive anomaly in the east of the basin (the generated salinity anomalies will partially compensate the effect of new temperature anomalies on density). In due time, the shape of the temperature anomaly approaches a cosine function in  $x$  (Fig. 12). By thermal wind balance, this new dipole-like temperature anomaly with a strong zonal gradient induces a northward current in the upper ocean, increasing MVT and leading to the transient strengthening of the AMOC (Fig. 8). Note that the temperature anomaly in the deep ocean (induced by the initial mixing from the surface) evolves relatively little, and nor there develops any substantial salinity anomaly.

The transient increase of MVT reveals a striking difference between the initial and subsequent effects of temperature and salinity anomalies on density. Specifically, in the very beginning of the evolution, the optimal initial SST and SSS anomalies are equivalent in modifying MVT and have a constructive role for the transient growth if both imposed. However later, after MVT reaches its maximum, density anomalies are mainly controlled

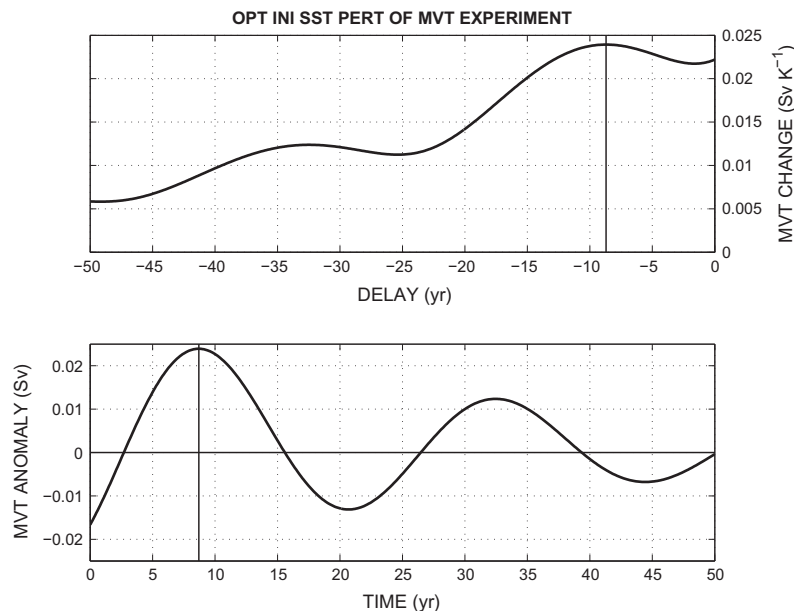


**Fig. 10.** (Top) The transient change in meridional volume transport (MVT) induced by optimal initial SST perturbations in the idealized model as a function of time delay. The thin vertical line indicates the most efficient or “most optimal” delay for modifying MVT. (Bottom) The evolution of the MVT after this optimal perturbation in SST was applied. The vertical line indicates the time when the perturbation has its maximum impact on MVT. For the mixing parameter  $p = 0.15$ .

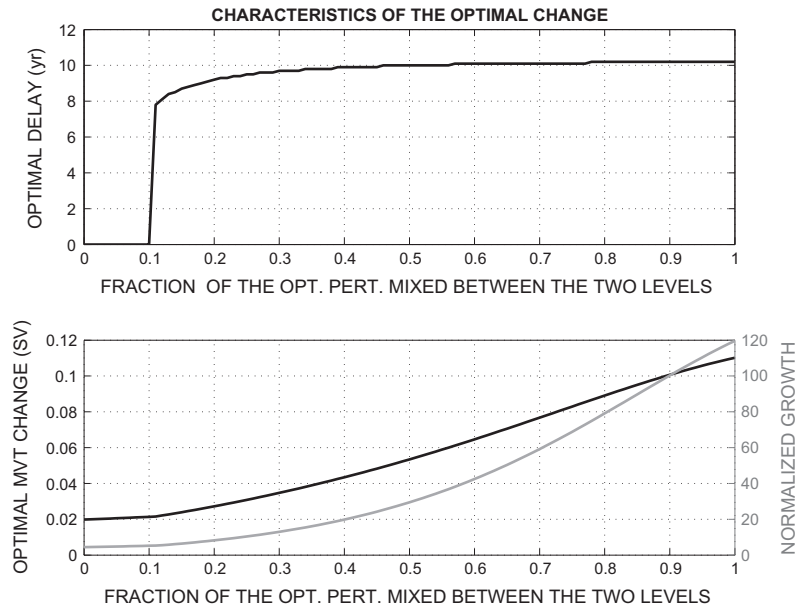


**Fig. 11.** The impact of the mixing parameter  $p$  on the characteristics of optimal transient change in the idealized model. (Top) The “most optimal” delay for the transient change as a function of  $p$ . (Bottom) The corresponding MVT change (black line) and the maximum normalized growth of density anomalies:  $\max_t(\langle \mathbf{u}_{id}(t) | \mathbf{S}_{id} | \mathbf{u}_{id}(t) \rangle) / \langle \mathbf{u}_{id}(0) | \mathbf{S}_{id} | \mathbf{u}_{id}(0) \rangle$  (grey line). The parameter  $p$  is introduced in expression (A8);  $p = 0$  means no deep mixing, whereas  $p = 1$  implies that the entire upper-ocean initial anomaly is immediately mixed between the two layers.

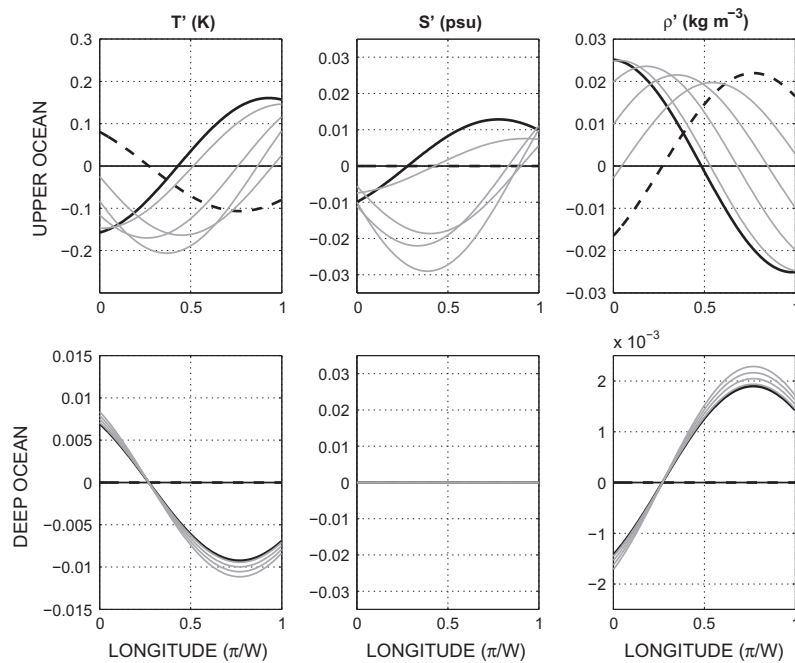


**Fig. 12.** Evolution of optimal SST perturbations in the idealized model. Dashed lines show the zonal structure of the anomalies at the initial time, heavy solid lines – at the time when the maximum MVT change is reached (8.8 yr after the perturbation was imposed), and light solid lines – at four intermediate times (2 yr, 4 yr, 6 yr, and 8 yr after). From left to right: the columns show temperature, salinity, and density anomalies multiplied by the relative thickness of the layers ( $h/H$  and  $\bar{h}/H$ , respectively). From top to bottom: the rows correspond to the upper and deep ocean. The cosine structure for density (the heavy solid line in the upper-right panel) gives the maximum MVT increase. Note the differences in scales between the top and bottom rows.

by temperature, with salinity partially counteracting the temperature effect (Fig. 12). This critical difference is a consequence of the nonnormality of the system ( $\mathbf{A}\mathbf{A}^\dagger - \mathbf{A}^\dagger\mathbf{A} \neq 0$ ).

This difference can be explained by considering the eigenmodes and biorthogonals of the idealized model. The change of MVT can only occur through the stimulation of the interdecadal mode and one of the purely-damped mode (i.e.  $|\mathbf{u}_{1,2}\rangle$  and  $|\mathbf{u}_5\rangle$ , respectively). The biorthogonals of these two modes ( $|\mathbf{u}_{1,2}^\dagger\rangle$  and  $|\mathbf{u}_5^\dagger\rangle$ ) ought to be density modes, where temperature and salinity work

constructively, because by definition they are orthogonal to all other eigenmodes (including  $|\mathbf{u}_{3,4}\rangle$  and  $|\mathbf{u}_6\rangle$ , which are spiciness modes). This demonstrates why density is so efficient in stimulating an MVT change.

In summary, the idealized model reveals that the transient growth arises from the optimal stimulation of two eigenmodes – the interdecadal mode and a purely-damped mode. By the time of the maximum change, the evolution of these two modes transforms the imposed density anomaly, initially located close

to the middle of the basin, into a density anomaly with a much more pronounced zonal gradient (Fig. 12), resulting in a change in the AMOC transport (since the east–west density gradient and MVT are tightly linked, e.g. Sévellec and Fedorov, 2013a). Thereafter, the excited interdecadal eigenmode continues to oscillate with an e-folding decay timescale of  $W^2/(\pi^2\kappa) = 36$  yr (Fig. 10). This timescale is controlled by horizontal diffusion and closely matches the timescale obtained from the ocean GCM (Fig. 6) as long as we use the same values of diffusivity in the full and idealized models. As discussed before, the period of the oscillation is determined by the westward propagation of anomalies across the basin due to the interplay between mean advection, geostrophic self-advection, and the  $\beta$ -effect.

## 5. Conclusions

How strongly can ocean temperature and salinity anomalies affect the Atlantic Meridional Overturning Circulation (AMOC)? This is an important question for climate science especially in the context of ongoing and future temperature and salinity changes in the North Atlantic. To address this question, in this study we have identified optimal initial perturbations for the AMOC within a realistic ocean GCM, i.e. such perturbations that could induce the greatest change in the overturning circulation. We used the meridional volume and heat transports by the Atlantic ocean (MVT and MHT, respectively) as quantitative measures of the AMOC and focused on perturbations in surface temperature and salinity fields (SST and SSS).

For both MVT and MHT experiments, the optimal surface temperature and salinity perturbations are associated with a large-scale density anomaly centered off the east coasts of Greenland and Canada. Using the ocean GCM together with an idealized model, we have shown that the transient growth of the AMOC arises from a nonnormal evolution of this density anomaly, which results in growing and then decaying temperature variations across the North Atlantic. For the MVT and MHT experiments, respectively, the most efficient optimal perturbations lead to the maximum transient change 8.9 and 7.8 yr after the perturbation was applied. The spatial pattern of the optimal initial perturbations remains similar and robust throughout all the 16 sets of experiments we conducted (despite different particular details of the problem formulation), which highlights the importance of the Atlantic subpolar regions for AMOC variability.

The physical mechanism of the transient change includes four stages: (1) A positive density anomaly ( $\rho' > 0$ , due to optimal SST or SSS perturbations) is imposed at the surface layer of the North Atlantic Ocean and is partially mixed into the deep ocean by convection (Fig. 8). (2) The resultant density anomaly induces a northward geostrophic flow along its eastern flank and a southward flow along the basin western boundary. (3) The anomalous flow interacts with the mean meridional gradient of temperature ( $\partial_y \bar{T} < 0$ ) and induces a dipole-like anomaly of temperature with a warming to the east and a cooling to the west of the initial density anomaly. (4) This dipole-like temperature anomaly creates a positive zonal density gradient in the upper ocean ( $\partial_x T' > 0$ ) which, by thermal wind balance, induces an anomalous northward flow in the upper ocean and a southward flow in the deep ocean. The latter effect is equivalent to a transient increase in the Atlantic meridional overturning (and hence in meridional volume and heat transports). After the maximum change is reached, temperature anomalies keep propagating westward in the upper Atlantic ocean, leading to a damped interdecadal oscillation.

The existence of a pronounced meridional temperature gradient in the upper ocean and its near absence in the deep ocean provide a source of nonnormality in the system crucial for the transient change. Another essential factor is oceanic deep convection that

communicates surface anomalies to the deep ocean, which explains why the optimal initial SST and SSS anomalies are centered in the region of deep mixed layer in the ocean GCM. This finding is corroborated by our idealized model which confirms the importance for the transient growth of how much the imposed surface anomalies are mixed into the deep ocean. Specifically, optimal delays exist in the idealized model only for  $p \geq 0.13$ , where  $p$  is the mixing parameter indicating how much surface anomalies are mixed between the ocean upper and the deep layers.

The sensitivity of the AMOC to perturbations in the deep ocean is consistent with the results of Zanna et al. (2011) obtained in a more idealized configuration (a symmetrical with respect to the equator rectangular basin with a flat bottom). While Hawkins and Sutton (2011) observed the strongest sensitivity at around 650 m depth in a coupled GCM (to simplify the problem they truncated the essential dynamics to several EOFs), Sévellec and Fedorov (2013b) used the same ocean GCM as in the present study and found that surface temperatures are most sensitive to perturbations at about 3700 m depth.

We have also explored the role of surface boundary conditions in setting the magnitude and timescale of the transient change induced by optimal perturbations. We find that the transient change due to salinity perturbations is only weakly sensitive to the choice of boundary conditions. However, the magnitude of the transient change caused by SST perturbations is significantly reduced when switching from the flux to mixed boundary conditions. The duration of the transient growth is also reduced but very slightly. The main reason for these differences between the evolution of SSS and SST perturbations is the strong damping of surface temperature anomalies under the mixed boundary conditions. We anticipate that the effective SST damping in coupled models should lie between our FBC and MBC experiments.

For the flux boundary conditions, this study shows that the optimal SST and SSS perturbations, rescaled in terms of density, induce similar transient changes in the AMOC and act on similar timescales. Using typical values for temperature or salinity anomalies observed in the North Atlantic one can estimate ensuing changes in the overturning strength. According to our calculations, anomalies of +1 K over the upper 500 m of the ocean (appropriate for global warming trends, Thierry et al., 2008) and  $-0.5$  psu over 250 m (appropriate for the Great Salinity Anomaly, Belkin et al., 1998) will lead to changes in the AMOC of  $-1.8$  Sv and  $-1.3$  Sv, respectively (14% and 10% of the mean overturning in the ocean GCM we used). These values are obtained by treating perturbations in temperature and salinity as the problem's initial conditions, but persistent perturbations could induce a much stronger AMOC response.

The accuracy of the linear framework for perturbations of similar magnitudes has been validated by Sévellec et al. (2008). In their study based on an ocean GCM with a slightly weaker mean overturning circulation, errors in the evolution of the optimal perturbations due to nonlinear effects were smaller than 14%. However, Sévellec et al. (2008) tested only linear initial perturbations; that is, optimal initial perturbations computed within a linear framework. To check the accuracy of the obtained optimal perturbations in a fully nonlinear context, one should consider more advanced methods, such as the Conditional Nonlinear Optimal Perturbations (e.g. Mu et al., 2004), but the latter method is not extensively developed yet for the use with ocean GCMs.

Our study has several implications for decadal predictability of the ocean meridional overturning circulation in the Atlantic. Firstly, our results imply that the spread predictions of the volume and heat transports by the AMOC is affected most by the same physical process: the excitation of zonal dipole-like SST patterns by initial density anomalies. In this paper we have described several key factors important for this process, including the best location of the initial anomalies for modifying the AMOC efficiently.

Secondly, the spatial patterns of the optimal initial perturbations can serve as precursors of future changes in the AMOC, especially given the robustness of these patterns in our experiments. In general, only those SST and SSS perturbations that have a nonzero projection on the optimal perturbations will be able to impact the AMOC after the optimal time delay. This implies that to anticipate AMOC changes approximately one decade in advance we should carefully monitor surface density changes in the Atlantic north of 50°N (over the region highlighted in Fig. 3). Such data targeting approaches can significantly reduce forecast errors, as shown by Zhou and Mu (2011) and Qin and Mu (2011) in the context of typhoon track forecasts. Similarly, to explain the weakening of the AMOC in the winter of 2009/2010 for example, one might need to search for causes possibly a decade earlier.

In conclusion we should mention that, even though we have discussed the role of different types of surface boundary conditions for the optimal response of the AMOC, this study has focused solely on ocean dynamics in a forced model. The next step is to consider the role of ocean–atmosphere interactions. The relevant questions include: How much would the damping of SST anomalies by ocean–atmosphere feedbacks reduce the transient change? Can the coupling between the ocean and the atmosphere modify the timescales of the transient change? Could synoptic atmospheric noise induce the transient growth and sustain interdecadal variability? These questions will be addressed in our future work.

### Acknowledgment

This research was supported by Grants from DOE Office of Science (DE-SC0007037), the David and Lucile Packard Foundation, and the Ti Ammo project funded through the French CNRS/INSU/LEFE program.

### Appendix A. Analysis of the idealized model

Applying the Fourier transform with respect to  $x$  to the set of Eqs. (11) and using (12) reduce the idealized model to

$$d_t | \mathbf{u}_{id} \rangle = \mathbf{A}_{id} | \mathbf{u}_{id} \rangle, \quad (\text{A1})$$

with

$$\langle \mathbf{u}_{id} | = \left( T_{cn}^u, T_{sn}^u, T_{cn}^d, T_{sn}^d, S_{cn}^u, S_{sn}^u, S_{cn}^d, S_{sn}^d \right),$$

and

$$\mathbf{A}_{id} = \begin{pmatrix} -\kappa \left( \frac{n\pi}{W} \right)^2 & A_{1,2} - \frac{n\pi}{W} \bar{u} & 0 & A_{1,4} & 0 & A_{1,6} & 0 & A_{1,8} \\ A_{2,1} + \frac{n\pi}{W} \bar{u} & -\kappa \left( \frac{n\pi}{W} \right)^2 & A_{2,3} & 0 & A_{2,5} & 0 & A_{2,7} & 0 \\ 0 & 0 & -\kappa \left( \frac{n\pi}{W} \right)^2 & 0 & 0 & 0 & 0 & 0 \\ 0 & 0 & 0 & -\kappa \left( \frac{n\pi}{W} \right)^2 & 0 & 0 & 0 & 0 \\ 0 & A_{5,2} & 0 & A_{5,4} & -\kappa \left( \frac{n\pi}{W} \right)^2 & A_{5,6} + \frac{n\pi}{W} \bar{u} & 0 & A_{5,8} \\ A_{6,1} & 0 & A_{6,3} & 0 & A_{6,5} - \frac{n\pi}{W} \bar{u} & -\kappa \left( \frac{n\pi}{W} \right)^2 & A_{6,7} & 0 \\ 0 & 0 & 0 & 0 & 0 & 0 & -\kappa \left( \frac{n\pi}{W} \right)^2 & 0 \\ 0 & 0 & 0 & 0 & 0 & 0 & 0 & -\kappa \left( \frac{n\pi}{W} \right)^2 \end{pmatrix},$$

where  $T_{cn}^u, T_{sn}^u, T_{cn}^d, T_{sn}^d, S_{cn}^u, S_{sn}^u, S_{cn}^d, S_{sn}^d$  and  $S_{sn}^d$  are the Fourier coefficients ( $n = 1, 2, 3, \dots$ ),  $| \mathbf{u}_{id} \rangle$  is the state vector, and  $\mathbf{A}_{id}$  is the Jacobian Matrix of the idealized model. Using the Fourier coefficients we express temperature and salinity anomalies as

$$T_{\{u,d\}}^r = \sum_n T_{cn}^{r\{u,d\}} \cos \left( \frac{n\pi}{W} x \right) + T_{sn}^{r\{u,d\}} \sin \left( \frac{n\pi}{W} x \right),$$

$$S_{\{u,d\}}^r = \sum_n S_{cn}^{r\{u,d\}} \cos \left( \frac{n\pi}{W} x \right) + S_{sn}^{r\{u,d\}} \sin \left( \frac{n\pi}{W} x \right).$$

The nonzero terms in this matrix correspond to diffusion, advection by the mean flow, geostrophic self-advection, and the baroclinic

Rosby wave propagation. The terms describing the two latter effects are calculated as

$$A_{1,2} = -A_{2,1} = \frac{h}{\bar{h}} A_{1,4} = -\frac{h}{\bar{h}} A_{2,3} = -\frac{n\pi}{W} \left( \frac{\alpha g \bar{h} h}{2Hf} \partial_y \bar{T} - \frac{\alpha g \bar{h} h^2 \beta_f}{4Hf^2} \partial_z \bar{T} \right),$$

$$A_{1,6} = -A_{2,5} = \frac{h}{\bar{h}} A_{1,8} = -\frac{h}{\bar{h}} A_{2,7} = +\frac{n\pi}{W} \left( \frac{\beta g \bar{h} h}{2Hf} \partial_y \bar{T} - \frac{\beta g \bar{h} h^2 \beta_f}{4Hf^2} \partial_z \bar{T} \right),$$

$$A_{5,6} = -A_{6,5} = \frac{h}{\bar{h}} A_{5,8} = -\frac{h}{\bar{h}} A_{6,7} = +\frac{n\pi}{W} \left( \frac{\beta g \bar{h} h}{2Hf} \partial_y \bar{S} - \frac{\beta g \bar{h} h^2 \beta_f}{4Hf^2} \partial_z \bar{S} \right),$$

$$A_{5,2} = -A_{6,1} = \frac{h}{\bar{h}} A_{5,4} = -\frac{h}{\bar{h}} A_{6,3} = -\frac{n\pi}{W} \left( \frac{\alpha g \bar{h} h}{2Hf} \partial_y \bar{S} - \frac{\alpha g \bar{h} h^2 \beta_f}{4Hf^2} \partial_z \bar{S} \right),$$

where  $\bar{h} = H - h$  is the thickness of the deep level, and  $\beta_f = d_y f$  is the meridional gradient of the Coriolis parameter estimated for the northern Atlantic.

A linear stability analysis of this dynamical system yields eight eigenvalues:

$$\lambda_{1,2} = -\kappa \left( \frac{n\pi}{W} \right)^2 \pm i \frac{n\pi}{W} \times \left[ \bar{u} + \frac{g \bar{h} h}{2Hf} (\alpha \partial_y \bar{T} - \beta \partial_y \bar{S}) - \frac{g \bar{h} h^2 \beta_f}{4Hf^2} (\alpha \partial_z \bar{T} - \beta \partial_z \bar{S}) \right], \quad (\text{A2})$$

$$\lambda_{3,4} = -\kappa \left( \frac{n\pi}{W} \right)^2 \pm i \frac{n\pi}{W} \bar{u}, \quad (\text{A3})$$

and

$$\lambda_{5,6,7,8} = -\kappa \left( \frac{n\pi}{W} \right)^2. \quad (\text{A4})$$

The corresponding eigenmodes are:

$$| \mathbf{u}_{1,2} \rangle = \frac{1}{c} \begin{pmatrix} \pm i \left( \frac{g \bar{h} h}{2Hf} \partial_y \bar{T} - \frac{g \bar{h} h^2 \beta_f}{2Hf^2} \partial_z \bar{T} \right) \\ \frac{g \bar{h} h}{2Hf} \partial_y \bar{T} - \frac{g \bar{h} h^2 \beta_f}{2Hf^2} \partial_z \bar{T} \\ 0 \\ 0 \\ \pm i \left( \frac{g \bar{h} h}{2Hf} \partial_y \bar{S} - \frac{g \bar{h} h^2 \beta_f}{2Hf^2} \partial_z \bar{S} \right) \\ \frac{g \bar{h} h}{2Hf} \partial_y \bar{S} - \frac{g \bar{h} h^2 \beta_f}{2Hf^2} \partial_z \bar{S} \\ 0 \\ 0 \end{pmatrix}, \quad | \mathbf{u}_{3,4} \rangle = \frac{1}{2} \begin{pmatrix} \pm i \beta \\ \beta \\ 0 \\ 0 \\ \pm i \alpha \\ \alpha \\ 0 \\ 0 \end{pmatrix}, \quad (\text{A5})$$

$$| \mathbf{u}_5 \rangle = \frac{1}{\bar{u}} \begin{pmatrix} -\frac{\alpha g \bar{h}^2}{2Hf} \partial_y \bar{T} + \frac{\alpha g \bar{h}^2 h \beta_f}{2Hf^2} \partial_z \bar{T} \\ 0 \\ \hat{u} \\ 0 \\ -\frac{\alpha g \bar{h}^2}{2Hf} \partial_y \bar{S} + \frac{\alpha g \bar{h}^2 h \beta_f}{2Hf^2} \partial_z \bar{S} \\ 0 \\ 0 \\ 0 \end{pmatrix}, \quad | \mathbf{u}_6 \rangle = \frac{1}{\bar{u}} \begin{pmatrix} 0 \\ -\frac{\alpha g \bar{h}^2}{2Hf} \partial_y \bar{T} + \frac{\alpha g \bar{h}^2 h \beta_f}{2Hf^2} \partial_z \bar{T} \\ 0 \\ \hat{u} \\ 0 \\ -\frac{\alpha g \bar{h}^2}{2Hf} \partial_y \bar{S} + \frac{\alpha g \bar{h}^2 h \beta_f}{2Hf^2} \partial_z \bar{S} \\ 0 \\ 0 \end{pmatrix},$$

$$| \mathbf{u}_7 \rangle = \begin{pmatrix} \frac{\alpha g \bar{h}^2}{2Hf} \partial_y \bar{T} - \frac{\alpha g \bar{h}^2 h \beta_f}{2Hf^2} \partial_z \bar{T} \\ 0 \\ 0 \\ 0 \\ \frac{\alpha g \bar{h}^2}{2Hf} \partial_y \bar{S} - \frac{\alpha g \bar{h}^2 h \beta_f}{2Hf^2} \partial_z \bar{S} \\ 0 \\ \hat{u} \\ 0 \end{pmatrix}, \quad | \mathbf{u}_8 \rangle = \begin{pmatrix} 0 \\ \frac{\alpha g \bar{h}^2}{2Hf} \partial_y \bar{T} - \frac{\alpha g \bar{h}^2 h \beta_f}{2Hf^2} \partial_z \bar{T} \\ 0 \\ 0 \\ 0 \\ \frac{\alpha g \bar{h}^2}{2Hf} \partial_y \bar{S} - \frac{\alpha g \bar{h}^2 h \beta_f}{2Hf^2} \partial_z \bar{S} \\ 0 \\ \hat{u} \end{pmatrix},$$



where  $\hat{u} = \bar{u} + c$  is the effective propagation velocity of eigenmodes 1 and 2,

$$c = \frac{g\tilde{h}h}{2Hf} (\alpha\partial_y\bar{T} - \beta\partial_y\bar{S}) - \frac{g\tilde{h}h^2\beta_f}{2Hf^2} (\alpha\partial_z\bar{T} - \beta\partial_z\bar{S}).$$

This propagation velocity,  $\hat{u}$ , includes advection by the mean flow,  $\bar{u}$ , geostrophic self-advection (the first two terms in the expression for  $c$ ), and the baroclinic Rossby wave propagation due to the  $\beta$ -effect. Eigenmodes 3 and 4 describe a spiciness mode passively advected by the mean flow. This spiciness mode has no direct impact on the density field and hence ocean circulation. The first four eigenmodes are related to processes in the upper ocean.

Among other four eigenmodes only one (mode 5) can influence the ocean meridional overturning. This is because modes 6 and 8 are also spiciness modes, whereas mode 7 (as well as 8) is associated with a full sine and, therefore, has a zero east–west density gradient and hence no MVT signature.

We can also compute the biorthogonals of these eigenmodes. For the norm, we choose the Euclidian scalar product, allowing a conventional decomposition:  $\mathbf{A}_{id} = \sum_{i=1}^8 |\mathbf{u}_i\rangle\lambda_i\langle\mathbf{u}_i^\dagger|$ . Henceforth, we obtain:

$$|\mathbf{u}_{1,2}^\dagger\rangle = \frac{1}{\hat{u}} \begin{pmatrix} \pm i\alpha\hat{u} \\ \alpha\hat{u} \\ \pm i\alpha\frac{\tilde{h}}{h}c \\ \alpha\frac{\tilde{h}}{h}c \\ \mp i\beta\hat{u} \\ -\beta\hat{u} \\ \mp i\beta\frac{\tilde{h}}{h}c \\ -\beta\frac{\tilde{h}}{h}c \end{pmatrix}, \quad |\mathbf{u}_{3,4}\rangle = \frac{1}{c} \begin{pmatrix} \mp i\left(\frac{g\tilde{h}h}{2Hf}\partial_y\bar{S} - \frac{g\tilde{h}h^2\beta_f}{2Hf^2}\partial_z\bar{S}\right) \\ -\left(\frac{g\tilde{h}h}{2Hf}\partial_y\bar{S} - \frac{g\tilde{h}h^2\beta_f}{2Hf^2}\partial_z\bar{S}\right) \\ 0 \\ 0 \\ \pm i\left(\frac{g\tilde{h}h}{2Hf}\partial_y\bar{T} - \frac{g\tilde{h}h^2\beta_f}{2Hf^2}\partial_z\bar{T}\right) \\ \frac{g\tilde{h}h}{2Hf}\partial_y\bar{T} - \frac{g\tilde{h}h^2\beta_f}{2Hf^2}\partial_z\bar{T} \\ 0 \\ 0 \end{pmatrix}, \quad (A6)$$

$$|\mathbf{u}_5^\dagger\rangle = \begin{pmatrix} 0 \\ 0 \\ 1 \\ 0 \\ 0 \\ 0 \\ 0 \\ 0 \end{pmatrix}, \quad |\mathbf{u}_6^\dagger\rangle = \begin{pmatrix} 0 \\ 0 \\ 0 \\ 1 \\ 0 \\ 0 \\ 0 \\ 0 \end{pmatrix}, \quad |\mathbf{u}_7^\dagger\rangle = \begin{pmatrix} 0 \\ 0 \\ 0 \\ 0 \\ 0 \\ 0 \\ 1 \\ 0 \end{pmatrix}, \quad |\mathbf{u}_8^\dagger\rangle = \begin{pmatrix} 0 \\ 0 \\ 0 \\ 0 \\ 0 \\ 0 \\ 0 \\ 1 \end{pmatrix}.$$

To understand the transient behavior of the idealized model, we now perform a generalized stability analysis following the procedure outlined in Section 3. To that end, we define (i) the measure of the optimization problem or the cost function, (ii) an appropriate norm for the anomalies, and (iii) a projector for the idealized model.

Choosing MVT as the measure, we define the operator  $\langle\mathbf{F}_{id}|$  as

$$\langle\mathbf{F}_{id}| = \left( -\alpha\frac{gh}{f}, 0, -\alpha\frac{g\tilde{h}}{f}, 0, \beta\frac{gh}{f}, 0, \beta\frac{g\tilde{h}}{f}, 0 \right).$$

The norm,  $\mathbf{S}_{id}$ , is chosen as

$$\langle\mathbf{u}_{id}|\mathbf{S}_{id}|\mathbf{u}_{id}\rangle = \frac{h}{H} \left( \alpha^2 T_{cn}^u{}^2 + \alpha^2 T_{sn}^u{}^2 + \beta^2 S_{cn}^u{}^2 + \beta^2 S_{sn}^u{}^2 \right) + \frac{\tilde{h}}{H} \left( \alpha^2 T_{cn}^d{}^2 + \alpha^2 T_{sn}^d{}^2 + \beta^2 S_{sn}^d{}^2 + \beta^2 S_{sn}^d{}^2 \right). \quad (A7)$$

The projector,  $\mathbf{P}_{id}^{SST}$  or  $\mathbf{P}_{id}^{SSS}$ , is defined as

$$\mathbf{P}_{id}^{SST} = \begin{pmatrix} 1 - p\frac{\tilde{h}}{H} & 0 \\ 0 & 1 - p\frac{\tilde{h}}{H} \\ p\frac{\tilde{h}}{H} & 0 \\ 0 & p\frac{\tilde{h}}{H} \\ 0 & 0 \\ 0 & 0 \\ 0 & 0 \\ 0 & 0 \end{pmatrix} \quad \text{or} \quad \mathbf{P}_{id}^{SSS} = \begin{pmatrix} 0 & 0 \\ 0 & 0 \\ 0 & 0 \\ 0 & 0 \\ 1 - p\frac{\tilde{h}}{H} & 0 \\ 0 & 1 - p\frac{\tilde{h}}{H} \\ p\frac{\tilde{h}}{H} & 0 \\ 0 & p\frac{\tilde{h}}{H} \end{pmatrix}, \quad (A8)$$

depending on whether we search for optimal temperature or salinity perturbations. These projectors select SST or SSS anomalies and also enable the mixing of the initial perturbations between the model top and bottom levels with the ratio  $p$ . This mixing parameter represents ocean mean convection that allows the deep ocean to feel the effect of surface anomalies during the initial stages of the GCM experiments. For particular computations using the idealized model, we choose  $p = 0.15$ , except when testing the sensitivity of the results to this parameter.

We solve the optimization problem only for the gravest wave number ( $n = 1$ ). Since the corresponding mode has a spatial zero-mean by construction, we need not apply the corresponding constraint. The results of the optimization analysis are discussed in Section 4.

## References

Azel, O., Huck, T., de Verdière, A. Colin, 2006. The different nature of the interdecadal variability of the thermohaline circulation under mixed and flux boundary conditions. *Journal of Physical Oceanography* 36, 1703–1718.

Barreiro, M. et al., 2008. Abrupt climate changes: how freshening of the Northern Atlantic affects the thermohaline and wind-driven oceanic circulations. *Review of Earth Planet and Sciences* 36, 33–58.

Belkin, I.S. et al., 1998. Great salinity anomalies in the North Atlantic. *Progress in Oceanography* 41, 1–68.

Blanke, B., Delecluse, P., 1993. Variability of the tropical Atlantic ocean simulated by a general circulation model with two different mixed-layer physics. *Journal of Physical Oceanography* 23, 1363–1388.

Broecker, W.S. et al., 1990. A salt oscillator in the glacial Atlantic? 1. The concept. *Paleoceanography* 5, 469–477.

Bugnion, V., Hill, C., Stone, P.H., 2006a. An adjoint analysis of the meridional overturning circulation in a hybrid coupled model. *Journal of Climate* 19, 3751–3767.

Bugnion, V., Hill, C., Stone, P.H., 2006b. An adjoint analysis of the meridional overturning circulation in an ocean model. *Journal of Climate* 19, 3732–3750.

Cunningham, S. et al., 2007. Temporal variability of the atlantic meridional overturning circulation at 26.5°N. *Science* 317, 935–937.

Curry, R., Mauritzen, C., 2005. Dilution of the northern North Atlantic ocean in recent decades. *Science* 308, 1772–1774.

Curry, R., Dickson, B., Yashayaev, I., 2003. A change in freshwater balance of the Atlantic ocean over the past four decades. *Nature* 426, 826–829.

Czeschel, L., Marshall, D.P., Johnson, H.L., 2010. Oscillatory sensitivity of Atlantic overturning to high-latitude forcing. *Geophysical Research Letters* 37, L1060.

de Verdière, A. Colin, 1988. Buoyancy driven planetary flow. *Journal of Marine Research* 46, 215–265.

de Verdière, A. Colin, Huck, T., 1999. Baroclinic instability: an oceanic wavemaker for interdecadal variability. *Journal of Physical Oceanography* 29, 893–910.

Dickson, B. et al., 2002. Rapid freshening of the deep North Atlantic ocean over the past four decades. *Nature* 416, 832–837.

Dickson, R.R., Curry, R., Yashayaev, I., 2003. Recent changes in the North Atlantic. *Philosophical Transactions A* 361, 1917–1934.

Durack, P.J., Wijffels, S.E., 2010. Fifty-year trends in global ocean salinities and their relationship to broad-scale warming. *Journal of Climate* 23, 4342–4362.

Farrell, B.F., Ioannou, P.J., 1996a. Generalized stability theory. Part I: autonomous operators. *Journal of the Atmospheric Sciences* 53, 2025–2040.

Farrell, B.F., Ioannou, P.J., 1996b. Generalized stability theory. Part II: nonautonomous operators. *Journal of the Atmospheric Sciences* 53, 2041–2053.

Farrell, B.F., Ioannou, P.J., 2001. Accurate low-dimensional approximation of the linear dynamics of fluid flow. *Journal of the Atmospheric Sciences* 58, 2771–2789.

Farrell, B.F., Moore, A.M., 1992. An adjoint method for obtaining the most rapidly growing perturbation to oceanic flows. *Journal of Physical Oceanography* 22, 338–349.

- Fedorov, A.V. et al., 2004. The effect of salinity on the wind-driven circulation and the thermal structure of the upper ocean. *Journal of Physical Oceanography* 34, 1949–1966.
- Fedorov, A.V. et al., 2007. The freshening of surface waters in high latitudes: effects on the thermohaline and wind-driven circulations. *Journal of Physical Oceanography* 37, 896–907.
- Gagosian, R.B., 2003. Abrupt climate change, should we be worried? Woods Hole Oceanographic Institution, World Economic Forum, 1–15.
- Ganachaud, A., Wunsch, C., 2000. Improved estimates of global ocean circulation, heat transport and mixing from hydrographic data. *Nature* 408, 453–457.
- Gent, P.R., McWilliams, J.C., 1990. Isopycnal mixing in ocean circulation model. *Journal of Physical Oceanography* 20, 150–155.
- Hansen, J. et al., 1999. GISS analysis of surface temperature change. *Journal of Geophysical Research* 104, 30997–31022.
- Hátún, H. et al., 2005. Influence of the Atlantic subpolar gyre on the thermohaline circulation. *Science* 309, 1841–1844.
- Hawkins, E., Sutton, R., 2009. Decadal predictability of the Atlantic ocean in a coupled GCM: forecast skill and optimal perturbations using linear inverse modeling. *Journal of Climate* 22, 3960–3978.
- Hawkins, E., Sutton, R., 2011. Estimating climatically relevant singular vectors for decadal predictions of the Atlantic Ocean. *Journal of Climate* 24, 109–123.
- Heimbach, P. et al., 2011. Timescales and regions of the sensitivity of atlantic meridional volume and heat transport: toward observing system design. *Deep Sea Research Part II: Topical Studies in Oceanography* 58, 1858–1879.
- Huck, T., Vallis, G.K., 2001. Linear stability analysis of three-dimensional thermally-driven ocean circulation: application to interdecadal oscillations. *Tellus* 53A, 526–545.
- Huck, T., de Verdière, A. Colin, Weaver, A.J., 1999. Interdecadal variability of the thermohaline circulation in box-ocean models forced by fixed surface fluxes. *Journal of Physical Oceanography* 29, 865–892.
- Josey, S.A., Marsh, R., 2005. Surface freshwater flux variability and recent freshening of the North Atlantic in the eastern subpolar gyre. *Journal of Geophysical Research* 110, C05008.
- Levitus, S., 1989. Interpentadal variability of temperature and salinity at intermediate depths of the North Atlantic ocean, 1970–1974 versus 1955–1959. *Journal of Geophysical Research* 94, 9679–9685.
- Madec, G., Imbard, M., 1996. A global ocean mesh to overcome the North Pole singularity. *Climate Dynamics* 12, 381–388.
- Madec, G. et al., 1998. OPA 8.1 Ocean General Circulation Model reference manual. Tech. rep., Institut Pierre-Simon Laplace (IPSL), France, No11, p. 91.
- Mann, M.E., Bradley, R.S., Hughes, M.K., 1999. Northern hemisphere temperature during the past millenium: inferences, uncertainties, and limitations. *Geophysical Research Letters* 26, 759–762.
- Marotzke, J. et al., 1999. Construction of the adjoint MIT ocean general circulation model and application to Atlantic heat transport sensitivity. *Journal of Geophysical Research* 104, 529–548.
- Marotzke, J., Welander, P., Willebrand, J., 1988. Instability and multiple steady states in a meridional-plane model of the thermohaline circulation. *Tellus* 40A, 162–172.
- Marti, O. et al., 2010. Key features of the IPSL ocean atmosphere model and its sensitivity to atmospheric resolution. *Climate Dynamics* 34, 1–26.
- Moore, A.M. et al., 2003. The role of air–sea interaction in controlling the optimal perturbations of low-frequency tropical coupled ocean–atmosphere modes. *Journal of Climate* 16, 951–968.
- Mu, M., Sun, L., Dijkstra, H.A., 2004. The sensitivity and stability of the ocean's thermohaline circulation to finite amplitude perturbations. *Journal of Physical Oceanography* 34, 2305–2315.
- Nolan, D.S., Farrell, B.F., 1999. The intensification of two-dimensional swirling flows by stochastic asymmetric forcing. *Journal of Atmospheric Sciences* 56, 3937–3962.
- Palmer, T.N., 1999. A nonlinear dynamical perspective on climate prediction. *Journal of Climate* 12, 575–591.
- Qin, X., Mu, M., 2011. Influence of conditional nonlinear optimal perturbations sensitivity on typhoon track forecasts. *Quarterly Journal of the Royal Meteorological Society*. <http://dx.doi.org/10.1002/qj.902>.
- Rahmstorf, S., 2002. Ocean circulation and climate during the past 120,000 years. *Nature* 419, 207–214.
- Redi, M.H., 1982. Oceanic isopycnal mixing by coordinate rotation. *Journal of Physical Oceanography* 12, 1154–1158.
- Reynolds, R.W., Smith, T.M., 1994. Improved global sea surface temperature analyses using optimum interpolation. *Journal of Climate* 7, 929–948.
- Rivière, G., Hua, B.L., Klein, P., 2001. Influence of the beta-effect on non-modal baroclinic instability. *Quarterly Journal of the Royal Meteorological Society* 127, 1375–1388.
- Sévellec, F. et al., 2008. Optimal surface salinity perturbations of the meridional overturning and heat transport in a global ocean general circulation model. *Journal of Physical Oceanography* 38, 2739–2754.
- Sévellec, F. et al., 2009. Nonnormal multidecadal response of the thermohaline circulation induced by optimal surface salinity perturbations. *Journal of Physical Oceanography* 39, 852–872.
- Sévellec, F., Fedorov, A.V., 2010. Excitation of SST anomalies in the eastern equatorial Pacific by oceanic optimal perturbations. *Journal of Marine Research* 68, 1–28.
- Sévellec, F., Fedorov, A.V., 2011. Stability of the Atlantic meridional overturning circulation in a zonally-averaged ocean model: the effects of freshwater flux, wind stress, and diapycnal diffusion. *Deep-Sea Research* 58, 1927–1943.
- Sévellec, F., Fedorov, A.V., 2013a. The leading, interdecadal eigenmode of the Atlantic meridional overturning circulation in a realistic ocean model. *Journal of Climate* 26, 2160–2183.
- Sévellec, F., Fedorov, A.V., 2013b. Model bias reduction and the limits of oceanic decadal predictability: importance of the deep ocean. *Journal of Climate* 26, 3688–3707.
- Sévellec, F., Ben Jelloul, M., Huck, T., 2007. Optimal surface salinity perturbations influencing the thermohaline circulation. *Journal of Physical Oceanography* 37, 2789–2808.
- Sirkes, Z., Tziperman, E., 2001. Identifying a damped oscillatory thermohaline mode in a general circulation model using an adjoint model. *Journal of Physical Oceanography* 31, 2297–2305.
- Srokosz, M. et al., 2012. Past, present, and future changes in the atlantic meridional overturning circulation. *Bulletin of the American Meteorological Society* 93, 1663–1676.
- Strogatz, S.H., 1994. *Nonlinear Dynamics and Chaos with Applications to Physics, Biology, Chemistry and Engineering*. Advanced book program, Perseus book, p. 498.
- Talley, L.D., Reid, J.L., Robbins, P.E., 2003. Data-based meridional overturning streamfunctions for the global ocean. *Journal of Climate* 16, 3213–3226.
- te Raa, L.A., Dijkstra, H.A., 2002. Instability of the thermohaline ocean circulation on interdecadal timescales. *Journal of Physical Oceanography* 32, 138–160.
- Thierry, V., de Boissesson, E., Mercier, H., 2008. Interannual variability of the Subpolar Mode Water properties over the Reykjanes Ridge during 1990–2006. *Journal of Geophysical Research* 113, C04016.
- Tziperman, E., 1997. Inherently unstable climate behaviour due to weak thermohaline ocean circulation. *Nature* 386, 592–595.
- Tziperman, E., Ioannou, P.J., 2002. Transient growth and optimal excitation of thermohaline variability. *Journal of Physical Oceanography* 32, 3427–3435.
- Tziperman, E., Zanna, L., Penland, C., 2008. Nonnormal thermohaline circulation dynamics in a coupled ocean–atmosphere GCM. *Journal of Physical Oceanography* 38, 588–604.
- Vellinga, M., Wood, R.A., 2002. Global climatic impacts of a collapse of the Atlantic thermohaline circulation. *Climatic Change* 54, 251–267.
- Wang, C., Dong, S., Munoz, E., 2010. Seawater density variations in the North Atlantic and the Atlantic meridional overturning circulation. *Climate Dynamics* 34, 953–968.
- Weaver, A.T., Vialard, J., Anderson, D.L.T., 2003. Three- and four-dimensional variational assimilation with a general circulation model of the tropical Pacific Ocean. Part 1. Formulation, internal diagnostics and consistency checks. *Monthly Weather Review* 131, 1360–1378.
- Wright, D.G., Stocker, T.F., 1991. A zonally averaged ocean model for thermohaline circulation. Part I: model development and flow dynamics. *Journal of Physical Oceanography* 21, 1713–1724.
- Zanna, L. et al., 2010. The role of ocean dynamics in the optimal growth of tropical SST anomalies. *Journal of Physical Oceanography* 40, 983–1003.
- Zanna, L. et al., 2011. Optimal excitation of interannual Atlantic meridional overturning circulation variability. *Journal of Climate* 24, 413–427.
- Zanna, L., Tziperman, E., 2005. Nonnormal amplification of the thermohaline circulation. *Journal of Physical Oceanography* 35, 1593–1605.
- Zhang, R., Delworth, T., 2005. Simulated tropical response to a substantial weakening of the atlantic thermohaline circulation. *Journal of Climate* 18, 1853–1860.
- Zhou, F., Mu, M., 2011. The impact of verification area design on tropical cyclone targeted observations based on the CNOP method. *Advances in Atmospheric Sciences* 28, 997–1010.